AGU PUBLICATIONS

JGR

Journal of Geophysical Research: Solid Earth

RESEARCH ARTICLE
10.1002/2017JB014020

Key Points:
- Volcanic water vapor emissions were measured with passive differential optical absorption spectroscopy (DOAS) for the first time
- Exceptionally high water vapor emissions were detected at Sabancaya, most likely due to boiling-off of the hydrothermal system
- The DOAS method could be used to detect similar, preeruptive water vapor plumes at other volcanoes, thus improving eruption forecasts

Supporting Information:
- Supporting Information S1

Correspondence to:
C. Kern,
ckern@usgs.gov

Citation:
Kern, C., P. Masias, F. Apaza, K. A. Reath, and U. Platt (2017), Remote measurement of high preeruptive water vapor emissions at Sabancaya volcano by passive differential optical absorption spectroscopy, *J. Geophys. Res. Solid Earth*, *122*, 3540–3564, doi:10.1002/2017JB014020.

Received 23 JAN 2017
Accepted 28 APR 2017
Accepted article online 1 MAY 2017
Published online 21 MAY 2017

Remote measurement of high preeruptive water vapor emissions at Sabancaya volcano by passive differential optical absorption spectroscopy

Christoph Kern[1], Pablo Masias[2], Fredy Apaza[2], Kevin A. Reath[3], and Ulrich Platt[4]

[1]Cascades Volcano Observatory, U.S. Geological Survey, Vancouver, Washington, USA, [2]Observatorio Vulcanológico del Instituto Geológico, Minero y Metalúrgico, Arequipa, Peru, [3]Department of Earth and Atmospheric Sciences, Cornell University, Ithaca, New York, USA, [4]Institute for Environmental Physics, University of Heidelberg, Heidelberg, Germany

Abstract Water (H_2O) is by far the most abundant volcanic volatile species and plays a predominant role in driving volcanic eruptions. However, numerous difficulties associated with making accurate measurements of water vapor in volcanic plumes have limited their use as a diagnostic tool. Here we present the first detection of water vapor in a volcanic plume using passive visible-light differential optical absorption spectroscopy (DOAS). Ultraviolet and visible-light DOAS measurements were made on 21 May 2016 at Sabancaya Volcano, Peru. We find that Sabancaya's plume contained an exceptionally high relative water vapor abundance 6 months prior to its November 2016 eruption. Our measurements yielded average sulfur dioxide (SO_2) emission rates of 800–900 t/d, H_2O emission rates of around 250,000 t/d, and an H_2O/SO_2 molecular ratio of 1000 which is about an order of magnitude larger than typically found in high-temperature volcanic gases. We attribute the high water vapor emissions to a boiling-off of Sabancaya's hydrothermal system caused by intrusion of magma to shallow depths. This hypothesis is supported by a significant increase in the thermal output of the volcanic edifice detected in infrared satellite imagery leading up to and after our measurements. Though the measurement conditions encountered at Sabancaya were very favorable for our experiment, we show that visible-light DOAS systems could be used to measure water vapor emissions at numerous other high-elevation volcanoes. Such measurements would provide observatories with additional information particularly useful for forecasting eruptions at volcanoes harboring significant hydrothermal systems.

Plain Language Summary Volcanoes emit large amounts of water vapor, but these emissions are difficult to measure because they are immediately mixed into the atmosphere which also contains significant water vapor. Here we present a new technique for remote detection of volcanic water vapor output. Applying our technique to Sabancaya Volcano, Peru, in May 2016, we found that the volcano was emitting 10 times more water vapor than we expected based on typical gas compositions measured elsewhere. We now know that the volcano would erupt in November 2016, just 6 months after our measurements. We believe that hot magma rising within the volcano led to a boiling of groundwater beneath the surface, which in turn caused the high water vapor emission rates that we measured. We expect that, using our new technique, similar signals might be detected prior to eruptions at other volcanoes around the world, thus helping observatories improve eruption forecasts.

1. Introduction

Water (H_2O) is by far the most abundant volcanic volatile species. In fact, high-temperature volcanic gases from arc volcanoes typically contain at least an order of magnitude more H_2O than any other species [*Giggenbach*, 1996; *Gerlach*, 2004]. Besides H_2O, high-temperature volcanic gases are mostly made up of carbon dioxide (CO_2), sulfur dioxide (SO_2), and hydrogen sulfide (H_2S), along with a number of minor constituents that together typically make up less than 2% of emissions [*Gerlach*, 2004]. Despite its abundance, there are a number of challenges associated with accurately determining volcanic H_2O emission rates, and measurements of H_2O output are therefore relatively seldom reported.

Here we show how we were able to overcome these difficulties and present a novel approach to measuring water vapor in volcanic plumes using passive, visible-light differential optical absorption spectroscopy (DOAS). With this new method, we were able to capture unexpectedly high H_2O emissions from

Sabancaya Volcano (Peru) in May 2016. We interpret our measurements in the context of subsequent activity at Sabancaya and explain why monitoring H_2O emissions with DOAS could provide valuable information for eruption forecasting at high-elevation volcanoes in the future.

1.1. Water Vapor in Volcanic Plumes

As the most abundant volatile, H_2O controls many aspects of volcanic eruptions. Eruptions can be initiated by excess pressure developing in a magma chamber due to accumulation of water-rich magma at the chamber top [*Blake*, 1984]. As magma rises and the hydrostatic pressure decreases, water vapor is exsolved, expands, and accelerates the rising column [*Sparks*, 1978; *Woods*, 1995]. When magma reaches the surface, dissolved H_2O has largely partitioned to the gas phase and controls the explosivity of the eruption [*Wilson et al.*, 1980]. Water can also influence the generation of pyroclastic flows [*Carey and Sigurdsson*, 1989]. As the eruption progresses, the volatile content of the primitive melt critically impacts the total erupted mass required to relieve overpressure [*Bower and Woods*, 1997], thereby affecting when the eruption will end. Clearly, a lot can be learned about volcanic systems by analyzing their water vapor emissions during periods of effusive degassing and eruption.

Volcanogenic water vapor emitted into the lower atmosphere has negligible environmental impact due to the high natural tropospheric H_2O background. However, large eruptions, particularly those occurring at midlatitudes, can inject water vapor into the stratosphere. Here it acts as a strong greenhouse gas [*Solomon et al.*, 2010]. Though recent satellite observations indicate that direct injection of volcanic H_2O is not an efficient mechanism for stratospheric hydration [*Sioris et al.*, 2016], it is possible that very large eruptions (volcanic explosivity index $>$ 5) could influence the entrainment of tropospheric water vapor, or even seawater, into the stratosphere [*Joshi and Shine*, 2003; *Joshi and Jones*, 2009; *Löffler et al.*, 2016], and thus impact climate. Perhaps more importantly, the water content of an eruption column clearly impacts its thermal energy budget and vertical development [*Herzog et al.*, 1998], thus also affecting the downwind transport of erupted products.

Despite its importance in driving volcanic processes and its possible role as a diagnostic tool for detecting volcanic unrest, water vapor measurements are relatively underreported in the literature when compared with other major volatile components of volcanic gases such as CO_2, SO_2, and H_2S. In part, this is because water vapor emissions from volcanoes are often difficult to interpret due to the fact that not all water vapor emitted by volcanoes actually originates in the magma. Many volcanoes host hydrothermal systems, and magmatic fluids passing through these can incorporate meteoric water [*Hinkley et al.*, 1995; *Goff and McMurtry*, 2000; *Botcharnikov et al.*, 2003]. At some volcanoes, additional H_2O might originate from heated local seawater incorporated in the conduit [*Symonds et al.*, 1990].

Another complicating factor stems from difficulties in accurately measuring water vapor in volcanic plumes. Any form of direct sampling or direct analysis of volcanic water vapor is subject to errors induced by the pressure and temperature-dependency of the H_2O vapor pressure inside the sampling system [*Symonds et al.*, 1994; *Wiederhold*, 1997]. Changes in pressure and temperature often lead to condensation which, if not carefully accounted for, can skew a sample or buffer a direct measurement in an undesirable manner. There is also always the potential for contamination of a measurement or sample by atmospheric water vapor.

Many of these difficulties can be overcome by using a contact-free method of detection. Volcanic water vapor has been successfully measured using Fourier transform infrared (FTIR) spectroscopy. *Naughton et al.* [1969] first measured the infrared absorption of volcanic volatiles by aiming an infrared spectrometer at a lava fountain during the 1968 Kilauea eruption. *Burton et al.* [2000] measured H_2O/SO_2 ratios at Masaya Volcano, Nicaragua, using active-source open path FTIR. These ratios can then be multiplied by SO_2 emission rates obtained from correlation spectrometer or DOAS measurements to obtain H_2O emission rates. In 2004, *Oppenheimer and Kyle* [2008] were able to measure the relative abundances of a wide range of volcanic gases including H_2O emitted from Erebus Volcano, Antarctica, by pointing an FTIR spectrometer at the hot lava lake, and similar experiments have been conducted here and elsewhere since then. The main challenge with these types of measurements is finding an adequate source of infrared radiation—a lamp, lava lake, or lava flow is required. Passive FTIR measurements using either the Sun or solar radiation scattered in the atmosphere would be preferable but are significantly more difficult due to the fact that the entire atmospheric

column is probed (see next section). To our knowledge, the only scattered-light FTIR measurements of volcanic water vapor in the literature were reported by *Love et al.* [2000], but these relied on several relatively uncertain assumptions regarding the vertical atmospheric water vapor and temperature profiles and have yet to be reproduced.

Besides measuring volcanic H_2O in infrared absorption, several studies have recently attempted to quantify water emissions by measuring the scattering of radiation on water droplets suspended in volcanic gas plumes [*Matsushima and Shinohara*, 2006; *Girona et al.*, 2015; *Pering et al.*, 2017]. These techniques attempt to relate the scattering efficiency of liquid water droplets in the plume to the abundance of water vapor or total water. However, this relationship depends on numerous parameters such as the vent exit temperature, the volcanic gas composition, the concentration of sulfate aerosols and other condensation nuclei in the plume, the temperature and relative humidity of the background air that is mixed into the plume, and the observation geometry (e.g., solar zenith and azimuth angles). Though potentially viable for detecting relative variability on short time scales, these techniques are difficult to implement quantitatively and require very frequent calibration using other methods.

1.2. Water Vapor in the Atmosphere

A major difficulty in measuring volcanic H_2O degassing stems from the fact that the atmospheric water vapor background is quite large. In fact, the volcanic H_2O contribution to the global atmospheric budget is negligible compared to the current natural background concentration, which mainly stems from evaporation of large water bodies. Averaged globally, the vertical atmospheric water vapor column density (VCD) is approximately 8×10^{22} molecules/cm^2 [*Randel et al.*, 1996]. If all water vapor in this column is condensed and precipitated, its depth would amount to about 2.5 cm. However, due to the fact that the vapor pressure of water in liquid and solid state increases exponentially with temperature (Clausius-Clapeyron relation), the atmosphere's ability to hold water vapor is strongly dependent on air temperature. Therefore, the atmospheric water vapor distribution is highly variable on both vertical and latitudinal spatial scales. Latitudinal cross sections of the total water vapor column often show VCDs of less than 1×10^{22} molecules/cm^2 (equivalent to 3 mm liquid water) at the poles but at least an order of magnitude more than that at the equator [*Maurellis et al.*, 2000; *Ye et al.*, 2007]. Likewise, the water vapor VCD above a given location will typically vary with season as the air temperature changes [*Gaffen et al.*, 1992]. The water vapor concentration decreases rapidly with altitude in the troposphere [*Committee for the Extension of the U.S. Standard Atmosphere*, 1976; *Cahen et al.*, 1982; *Palchetti et al.*, 2007], as temperature also decreases. Strikingly, a temporary decrease in global average H_2O VCDs was even observed ensuing the 1991 eruption of Mount Pinatubo, as global-mean lower tropospheric temperature cooled by about a half degree Celsius for several years [*Soden et al.*, 2002].

As mentioned before, the vertical water vapor distribution can be approximated by an exponential decrease in concentration with altitude. The so-called "scale height" H of this distribution gives the altitude at which the concentration has dropped to $1/e$ times the concentration present at sea level. The water vapor scale height in the atmosphere typically varies between about 1 and 3 km, with the highest values observed in close proximity to large, high-temperature bodies of water where evaporation is most efficient [*Tomasi*, 1984; *Turner et al.*, 2001; *Wagner et al.*, 2013]. Away from major water vapor sources and sinks, a scale height of 2 km usually represents a good estimate [*International Telecommunication Union*, 2012]. Since the scale height of oxygen and nitrogen, the major constituents of the atmosphere, is approximately 8 km, by far the majority of the water vapor is located in the lowermost part of the atmosphere.

An approximation for the atmospheric H_2O VCD above a given altitude or topographic elevation h can be obtained by integrating the exponential concentration profile $c_{H2O}(z)$ from h to infinity.

$$\mathrm{VCD}(h) = \int_h^\infty c_{\mathrm{H2O}}(z)\, dz = \int_h^\infty c_0 e^{-\left(\frac{z}{H}\right)}\, dz = c_0\, H\, e^{-\left(\frac{h}{H}\right)} \quad (1)$$

At sea level, the VCD is therefore simply the concentration of water vapor c_0 times the scale height. The vertical column decreases very rapidly as the observer ascends in elevation. At 5000 m, for example, the VCD is less than 10% of the VCD measured at sea level for a scale height H of 2 km.

Based on these considerations, we will refer to a "standard atmosphere" throughout this manuscript as one that has an H_2O VCD of 8×10^{22} molecules/cm^2, an H_2O scale height of 2 km, an air scale height of 8 km, and an air concentration of 2.6×10^{19} molecules/cm^3 at sea level.

1.3. The Challenge of Measuring Water Vapor in Volcanic Plumes With Scattered-Light Remote Sensing

The global volcanic flux of water vapor into the atmosphere remains relatively poorly constrained [*Textor et al.*, 2004]. One reason for this is the fact that accurately quantifying volcanic H_2O emission rates is challenging. Up to now, all measurements of volcanic H_2O output have been based on an indirect measurement scheme. First, the relative chemical composition of volatile output is determined, either by petrologic analysis of relative volatile concentrations in extruded lava or by laboratory or direct analysis of the H_2O/SO_2 ratio in the emitted gases. In a second step, the H_2O flux is then derived from this composition and the lava extrusion rate or SO_2 emission rate measured by another technique. Methods measuring light scattered on condensed water droplets can derive the emission rate directly, but then rely on an indirect relationship between light-scattering and H_2O abundance.

Constraining the SO_2 emission rate is relatively straightforward because this species can readily be measured using scattered-light remote sensing and its atmospheric background is negligible. Today, DOAS is commonly used to measure the absorption of ultraviolet solar radiation as it passes through the volcanic plume. By scanning a DOAS instrument field of view across the plume or passing an upward looking instrument under the plume, the number of SO_2 molecules in a 1 m wide plume cross section can be determined (e.g., in molecules/m). This number, multiplied by the plume speed (e.g., in m/s), gives the SO_2 emission rate (e.g., in molecules/s).

The main difficulty in measuring volcanic H_2O and CO_2 in the same way lies in the nonnegligible atmospheric background concentrations of these gases. Since all scattered solar radiation has already passed through the entire atmospheric column to reach the detecting instrument, H_2O and CO_2 absorption signals are present regardless of whether the radiation has passed through a volcanic plume or not. In fact, the signal enhancement expected from a volcanic plume will normally be very small. A typical high-temperature plume from an active, quiescently degassing volcano might contain an SO_2 VCD of about 10^{18} molecules/cm^2. That same plume might contain 10^{20} H_2O molecules/cm^2, but this is only about 0.1% of the average atmospheric H_2O background VCD at sea level.

In this study, we aim to show that though difficult, measuring H_2O with scattered-light DOAS is not actually impossible. By selecting a favorable, very high volcano located in an unusually dry region with an above-average H_2O flux, we were able to measure the volcanic H_2O emission rate with DOAS for the first time. Though clearly a special case study, we argue that the technique is indeed applicable to a number of high-altitude volcanoes around the world and that the additional insights we stand to gain make the task well worth pursuing.

2. Instrument Setup and Study Site

In this section, the instrumentation and methods that were used to perform DOAS measurements of H_2O are described. DOAS measurements were made in both vehicle-based traverse and stationary scanning geometries at Sabancaya Volcano, Peru. In addition to the visible (Vis) spectral range used for H_2O analysis, all measurements also included the ultraviolet (UV) spectral region so that SO_2 column densities and emission rates could be retrieved. The SO_2 emissions give background information on Sabancaya's level of activity during the measurements and provide context for comparing the H_2O retrievals and results presented later on in sections 3 and 4.

2.1. Sabancaya Volcano, Peru

Sabancaya Volcano is an active stratovolcano located in the central Andean volcanic zone in southern Peru (Figure 1). With a summit elevation of 5967 m, it is slightly lower than the 6288 m dormant Ampato Volcano located just 4 km to its immediate southwest and part of the same complex [*Samaniego et al.*, 2016]. Prior to its current crisis, Sabancaya last experienced a violent eruption in May–June 1990 followed

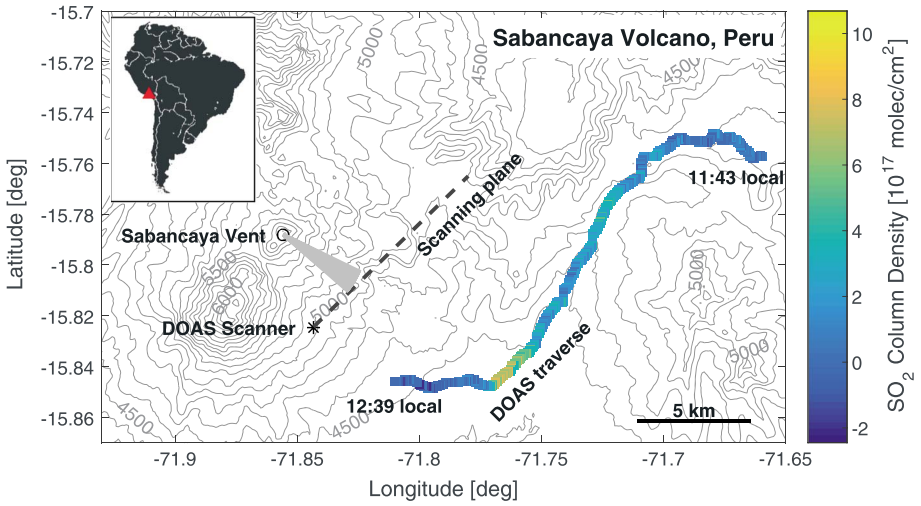

Figure 1. Topographic map of Sabancaya Volcano, Peru, and the surrounding area. A DOAS traverse beneath the gas plume was performed between 11:43 and 12:39 local time on 21 May 2016. The SO_2 column density measured above the vehicle during this traverse is shown. Up to about 1×10^{18} SO_2 molecules/cm^2 were detected. Also shown is the approximate plume direction (shaded area) and where the scanning measurements performed later that afternoon intersected the plume (dashed line). Topographic data from [*U.S. Geological Survey*, 2006].

by a period of 8 years with frequent vulcanian and phreatomagmatic events. The small volumes of juvenile tephra erupted during this time period were of andesitic to dacitic composition [*Gerbe and Thouret*, 2004].

Small explosions emitted gas and ash in 2000 and 2003, but the volcano then became quiet for a decade. This period of quiescence ended in February 2013, when an earthquake swarm damaged walls and bridges in an irrigation canal network on the Majes drainage. Around this time, gases also began emitting from fumaroles in the summit crater area, and SO_2 emissions picked up from essentially zero to several tens of metric tons per day (t/d) in 2013 and up to 1000 t/d in 2014, as measured by vehicle-based DOAS traverses of the plume. Beginning in 2016, a scanning DOAS network was installed as part of the Network for Observation of Volcanic and Atmospheric Change [*Galle et al.*, 2010], and emissions have since climbed to maximum values of over 6000 t/d. A number of fumaroles located away from the volcano's summit vent began visibly steaming in summer of 2016, with emissions appearing to increase in vigor over time. Finally, a series of minor explosions and continuous low-level ash emissions began on 6 November 2016, and on 11 November 2016, Sabancaya experienced an explosive eruption that sent an ash column up to 3 km above the volcano's summit. Unrest continues through the time of this writing.

The current crisis at Sabancaya poses limited hazards of ashfall to small communities surrounding the volcano. In particular, local alpaca and llama farmers are concerned for the health of their animals given the ashfall on grazing land. There are reports of cattle dying in proximal areas during the lead-up to the 1990 eruption, either from breathing noxious fumarolic gases or eating contaminated foliage [*de Silva and Francis*, 1990, and references therein]. If larger eruptions were to occur, the main associated hazards would stem from lahars, mudflows, and, to a lesser degree, pyroclastic and lava flows down the Rio Colca, Sihuas, and Majes drainages [*de Silva and Francis*, 1991]. The Observatorio Vulcanológico del Instituto Geológico, Minero y Metalúrgico (OVI) closely monitors Sabancaya. Hazard maps and reports on current activity can be found on their website (http://ovi.ingemmet.gob.pe).

2.2. DOAS Traverse Measurements

The measurements we report on in this study were recorded on 21 May 2016, when SO_2 emissions had not yet reached their current levels and the plume was still free of ash. Light winds carried the plume emitted from Sabancaya's summit toward the southeast. Access to the volcano is by unpaved dirt track from the east, so our vehicle passed beneath the plume during our approach of the volcano between 11:43 and 12:39 local time (Figure 1). During this time, the solar zenith and azimuth angles ranged from 36 to 39 and from 0 to 339°, respectively. Two zenith-looking telescopes were mounted on the truck, each coupling scattered solar

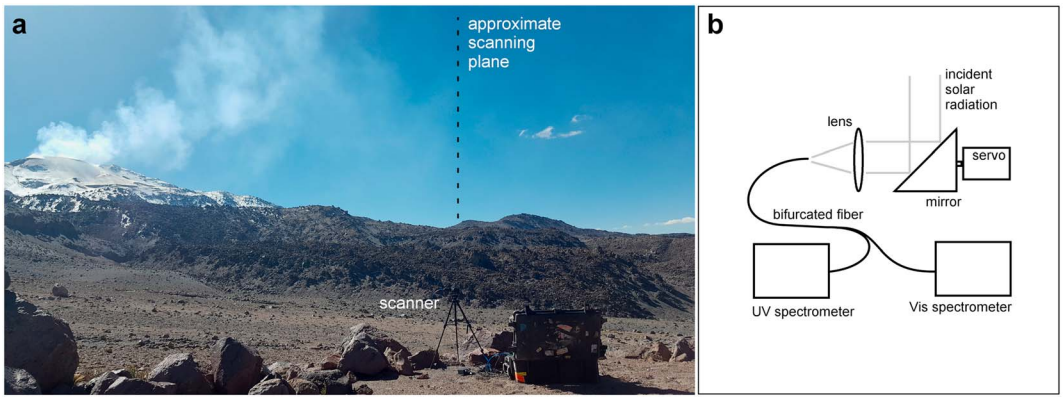

Figure 2. (a) Photograph of the scanning DOAS measurement setup on 21 May 2016. Mounted on a tripod, a scanner was used to scan across the plume emitted from Sabancaya in approximately perpendicular direction. The elevation angles of between 4 and 82° were stepped through in 3° increments. (b) Schematic of the optical setup. Light reflected on the scanner's mirror was coupled into a bifurcated fiber leading to UV and Vis spectrometers.

radiation from a narrow 1° field of view into separate fiber optic cables and into two different spectrometers. An Ocean Optics SD2000 UV spectrometer was used to measure the spectral radiance between 280 and 420 nm at a spectral resolution of 0.6 nm, and an Ocean Optics USB2000+ Vis spectrometer was used to measure the spectral radiance between 450 and 780 nm at a resolution of 1.2 nm. Using a compiled MATLAB code written for this purpose, data were acquired at 1 s integration time on two laptop computers, and GPS receivers were used to record the time and location of each acquisition.

2.3. Scanning DOAS Measurements

After the plume traverse was completed, scanning DOAS measurements were set up at a site 5 km south of Sabancaya's summit at 5040 m elevation (Figure 1). A small scanner was set on a tripod such that its scanning plane was approximately perpendicular to the direction of plume propagation (Figure 2). In the scanning unit, a servo motor successively positioned an aluminum-coated right-angle mirror such that scattered radiation was collected from elevation angles between 4 and 82° above the horizontal in steps of 3°. A 40 mm focal length fused silica lens coupled scattered radiation into a 2×600 μm diameter bifurcated fiber, thus collecting radiation from an ~0.9° field of view. The fibers led to two separate Ocean Optics USB2000+ spectrometers (Figure 2). Similar to the traverse setup, the two spectrometers covered the spectral ranges 280–430 nm and 450–780 nm at optical resolutions of 0.6 nm and 1.2 nm, respectively. Two laptops were again used to acquire data through the spectrometers' USB interfaces.

Prior to spectral analysis, the data acquired on the two separate spectrometer systems were synchronized according to the time stamps provided by GPS receivers connected to each laptop. The computer controlling the Vis spectrometer also controlled the scanner, positioning the latter such that a Vis spectrum with 5 s integration time could be recorded at each elevation angle. The start and stop time of each Vis measurement was saved. UV spectra were recorded coincidentally on the other system at 1 s integration times. These were later sorted such that successive UV spectra recorded during a particular Vis acquisition were co-added and UV spectra recorded while the scanner was moving were discarded. This procedure resulted in a time series of UV and Vis spectra recorded at coincident times and viewing geometries.

The scanning measurements ran from 14:11 to 16:11 local time. During this interval, measurement conditions were ideal for UV/Vis remote sensing. The solar zenith and azimuth angles ranged from 51 to 75° and 314 to 297°, respectively. Only very few, very small meteorological clouds were in the area and did not interfere with measurements. Perceptible visibilities were in excess of 80 km based on the discernibility of surrounding topography when viewed from the measurement site.

2.4. SO_2 Emissions From Sabancaya

For the traverse measurements, the SO_2 VCD above the vehicle was retrieved from the collected UV spectra by performing a standard DOAS evaluation [*Galle et al.*, 2002; *Platt and Stutz*, 2008]. For this, the measurement

Table 1. Retrieval Parameters Used in This Study for the DOAS Analysis of SO_2, O_4, and H_2O[a]

DOAS Retrieval Parameter	Value
All evaluations	
Spectral corrections	Subtract dark current
	Subtract electronics offset
Calculation of optical depth	Divide by clear-sky or zenith spectrum
	Logarithm
SO_2 analysis	
Fit wavelength range	314–330 nm
Fit references	SO_2 [*Vandaele et al.*, 2009]
	O_3 [*Bogumil et al.*, 2003]
	Ring correction [*Grainger and Ring*, 1962]
	Wavelength calibration correction [*Beirle et al.*, 2013]
	Polynomial (third order)
O_4 analysis	
Fit wavelength range	560–610 nm
Fit references	O_4 [*Hermans*, 2010]
	O_3 [*Bogumil et al.*, 2003]
	H_2O [*Rothman et al.*, 2013]
	Ring correction [*Grainger and Ring*, 1962]
	Wavelength calibration correction [*Beirle et al.*, 2013]
	Polynomial (third order)
H_2O analysis	
Fit wavelength range	713–748 nm
Fit references	H_2O [*Rothman et al.*, 2013]
	Ring correction [*Grainger and Ring*, 1962]
	Wavelength calibration correction [*Beirle et al.*, 2013]
	Polynomial (third order)

[a]All spectral analyses were performed using the DOASIS software [*Kraus*, 2006]. All literature reference cross sections were convolved with the respective spectrometers' instrument line shape prior to fitting.

spectra were first corrected for detector dark current and electronic offset. The optical depth was calculated by dividing by a clear-sky reference and taking the negative of the logarithm of this ratio. Then, a number of precalculated reference spectra were fit to the measurement spectra in the 314–330 nm wavelength interval: (1) the high-resolution absorption cross sections of SO_2 [*Vandaele et al.*, 2009] and O_3 [*Bogumil et al.*, 2003] were convolved with the UV spectrometer's instrument line shape (obtained from a laboratory measurement of a mercury calibration lamp) to account for the spectrometer's optical resolution, (2) a Ring spectrum [*Grainger and Ring*, 1962] was calculated from the clear-sky spectrum using the DOASIS software [*Kraus*, 2006] to account for a variable contribution of Raman scattering to the measured spectra, (3) two references were prepared to correct for minor changes in the spectrometer's wavelength calibration during the course of the measurements following the recommendations of [*Beirle et al.*, 2013], and (4) a third-order polynomial was included in the fit to describe broadband variations in the spectrum. Table 1 summarizes this procedure as well as the similar retrievals of O_4 and H_2O discussed later on.

When applied to the spectra recorded during the vehicle traverse of the plume, the DOAS analysis yielded SO_2 column densities of up to 1×10^{18} molecules/cm^2. Measurement errors derived from the fit residual [*Stutz and Platt*, 1996] averaged 1×10^{17} molecules/cm^2. Though traces of SO_2 were encountered east of the vent, perhaps from swirling distal winds, the highest columns were clearly found at a location 10 km southeast of the active summit (Figure 1). From these, the near-field wind direction can be estimated at 300 ± 10° off north. Integrating the column densities obtained while traversing the main plume and multiplying by a wind speed of (4.1 ± 0.8) m/s (derived from video sequences recorded later at the scanning site, see below) yields an SO_2 emission rate of 800 ± 180 t/d. The error indicated here is calculated based on independent propagation of errors in the individual column densities, the plume direction and the plume speed.

The UV spectral data collected during our plume scans were analyzed for SO_2 absorption according to the same methodology. The results show that gas emissions from the summit and wind conditions were both relatively stable throughout the measurement period. The plume was generally detected in a swath of about 15° width. During the course of the measurements, its center position varied between 8 and 20° elevation.

The plume reached all the way down to the horizon in a few scans but not the majority. Variations in plume center position appeared to stem from small changes in the altitude of the lofting plume.

The wind direction of (300 ± 10°) was previously determined by a DOAS traverse conducted while approaching the scanning location (section 2.2). The wind speed was determined by recording a video of the plume from the DOAS scanner location at 15:11 local time. Though virtually invisible at the location of the scanning plane, it was possible to track visible plume features in closer proximity to the vent (Figure 2). Several features were tracked in video frames separated by 10 s each, and their location relative to stationary landmarks was determined. The hand-picked plume displacement averaged (1.57 ± 0.34) pixels per second which, when combined with an assumed plume distance of 3.4 km, a total sensor width of 1644 pixels and a camera horizontal viewing angle of 64.6°, yielded a wind speed of (4.1 ± 0.8) m/s.

SO_2 emission rates were obtained for the scanning measurements using the standard approach of integrating each scan and multiplying the retrieved SO_2 burdens with the wind speed [*Galle et al.*, 2002]. During the period of scanning measurements, the SO_2 emission rate averaged 890 t/d, with a standard deviation for individual scans of 240 t/d. Rather than assume a constant plume height for our calculations, we assumed a constant plume distance and integrated radially across the plume. We deem this approach to be less susceptible to errors given the apparent variability of plume height but relative stability of wind direction, though these observations stem solely from visual estimation of the plume geometry over time.

Analogous to the methods presented by *Kern et al.* [2009], the radiative transfer model McArtim [*Deutschmann et al.*, 2011] was used to examine the influence of light dilution on our measurements. In the absence of scattering aerosols, an assumption justified by the pristine atmospheric conditions observed during our measurement period, we found that our retrieved SO_2 column densities likely underestimate the true values by an average of ~10% due to light entering the instrument field of view without having passed through the plume. However, we chose not to correct our emission estimates because the correction would depend on the exact measurement geometry at a given time and would therefore vary over the course of the measurements as the plume height varies. We also found that the influence of light dilution on the H_2O column densities, measured in the visible region and discussed in the next section, was almost identical. Therefore, the H_2O/SO_2 ratios are not significantly affected and need not be corrected.

We estimate the variation of the plume height over time and the measurement error stemming from our assumption of a constant plume distance to be about ~10% as well. Furthermore, the spectroscopic error derived from the DOAS fit residual was also ~10% and independent of the other errors. However, the largest source of error for the emission rate stems from the uncertainty of the wind speed (~20%, see above). Taking all of these error sources into consideration, we estimate the total error on our derived SO_2 emission rate to be about 230 t/d, or 26% of the average value. Therefore, the recorded variability of emissions (240 t/d standard deviation) may simply be the result of variability in the plume geometry and wind speed during our measurement interval.

3. Measuring Water Vapor With DOAS

Though, to our knowledge, volcanic water vapor emissions have never before been measured by DOAS, the technique has been used extensively to measure total atmospheric water vapor column densities from both ground-based and satellite platforms [*Noël et al.*, 1999, 2004; *Wagner et al.*, 2003, 2013; *Sierk et al.*, 2004; *Lampel et al.*, 2015]. In the following, we discuss the geometric considerations that are necessary for evaluating passive DOAS measurements of localized water vapor plumes in the atmosphere. Then, the details of our spectral H_2O retrieval are outlined and the differences to evaluation schemes targeting atmospheric H_2O are discussed.

3.1. Geometric Approximation of Atmospheric Radiative Transfer

In comparison to the relatively straightforward evaluation of spectroscopic SO_2 measurements, the analysis of water vapor absorption measurements is complicated by the fact that the atmospheric background of water vapor is significant. In fact, any H_2O absorption signals measured with DOAS will typically be mainly associated with the natural background rather than a localized plume. Perhaps even more importantly, any change in the atmospheric radiative transfer, i.e., the distribution of light paths between the Sun and

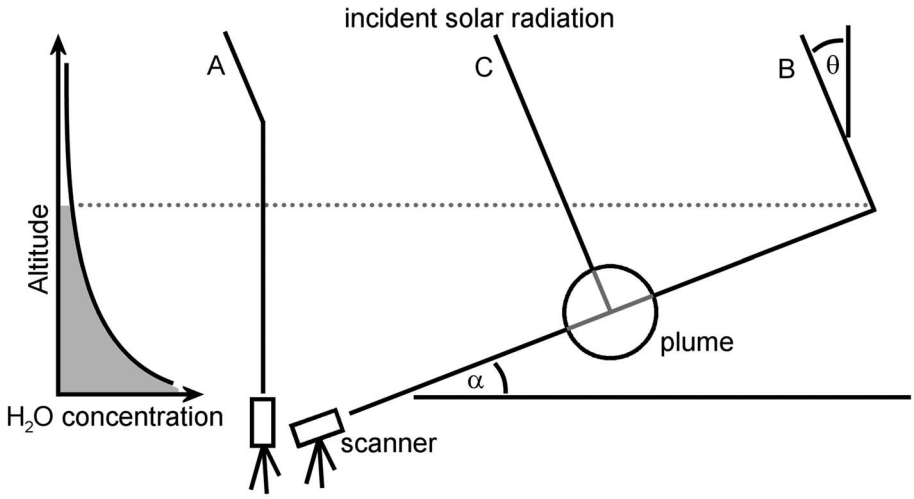

Figure 3. Schematic of the radiative transfer in the scanning DOAS measurements. Since the atmospheric concentration of H_2O decreases very rapidly with altitude, a zenith-looking instrument sees the VCD regardless of the solar zenith angle θ (path A). In geometrical approximation, all H_2O is close enough to the ground such that an instrument aimed at elevation angle α measures radiation last scattered above the H_2O layer (path B). The light path length in the H_2O layer is then proportional to 1/sin(α). This geometrical approximation could become inaccurate if light were scattered on aerosols in the plume (path C), as this last scattering event would potentially lie within the atmospheric H_2O layer.

the instrument, has the potential to affect the measured H_2O absorbance. Therefore, any spectroscopic measurements of water vapor can only be interpreted in the context of the measurement geometry.

For these discussions it is useful to define a number of terms typically used in the Multi-Axis DOAS community. The water vapor vertical column density (VCD) has already been defined as the total number of gas-phase H_2O molecules per unit area along a vertical path above the instrument. The water vapor slant column density (SCD) gives the number of gas-phase H_2O molecules per unit area along the effective light path through the atmosphere. The atmospheric light path is generally not a vertical column, which is particularly obvious when the instrument field of view is aimed at a nonzenith elevation angle α (Figure 3). The extension of the effective light path in the atmosphere over the vertical column is given by the so-called air mass factor (AMF).

$$\mathrm{SCD} = \mathrm{AMF} \cdot \mathrm{VCD} \tag{2}$$

In DOAS analyses, a given measurement spectrum is always evaluated relative to a reference spectrum. In the case of our scanning measurements, we evaluated all spectra in a particular scan relative to the most upward looking spectrum recorded in that scan. Therefore, we are measuring the enhancement of water vapor absorption over what is already contained in the reference spectrum. This value is called the differential slant column density (DSCD).

All the measurements collected in this study use scattered solar radiation as a light source. The interpretation of our measured DSCDs is aided by knowledge of where the recorded radiation was last scattered before arriving at the instrument. Due to the pristine nature of the atmosphere at the time of our measurements and the relatively low albedo of the terrain surrounding our study site, we can approximate atmospheric radiative transfer by assuming a pure Rayleigh atmosphere, i.e., an atmosphere in which radiative transfer is governed by scattering on air molecules. In this approximation, the atmospheric scattering coefficient is proportional to the density of air molecules, which decreases exponentially with altitude. Therefore, scattering will be most efficient close to the ground. However, if we compare the number of air molecules in the lowermost 2 km layer above the instrument with the number of molecules in the rest of the atmospheric column, we find that about 80% of molecules are located above 2 km, regardless of the altitude of the instrument. In single-scattering approximation, this means that ~80% of the detected radiation has passed through the lowermost 2 km of the atmosphere in a straight line along the instrument's viewing direction, regardless of the measurement elevation angle α. Since the water vapor scale height is only 2 km, by far

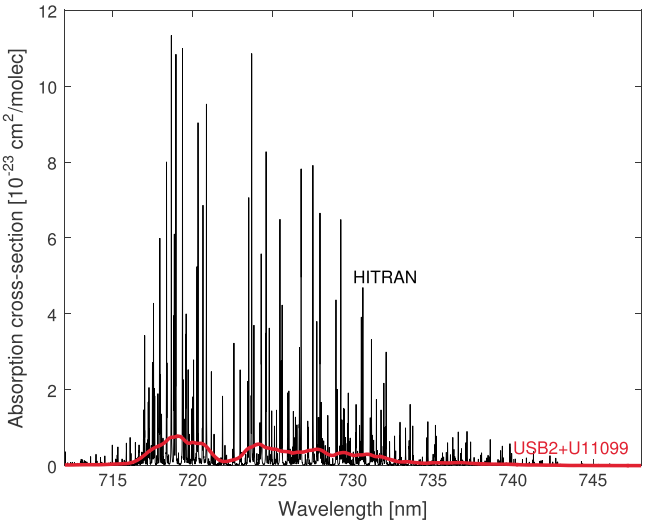

Figure 4. The water vapor absorption band around 720 nm was chosen for our spectral retrieval. Convolution of the HITRAN2012 absorption cross section (black [*Rothman et al.*, 2013]) with our instrument slit function yields the expected response of our spectrometer (red). Because individual absorption lines cannot be resolved, the instrument response is slightly nonlinear in water vapor column density (see text for details).

the majority of the detected radiation has passed through the relatively thin water vapor layer in a straight line.

In cases like this, where the detected scattered radiation mainly passes through a proximal trace gas layer along a straight path, the respective AMF is given by a simple geometric approximation and depends only on the elevation angle α of the measurement.

$$\mathrm{AMF} = 1/\sin(\alpha) \tag{3}$$

This geometrical approximation of the AMF greatly simplifies the interpretation of scattered-light DOAS data. We verified its applicability to our measurements by comparing the geometrical AMFs (equation (3)) to AMFs calculated using the McArtim radiative transfer model [*Deutschmann et al.*, 2011] initialized with our approximate measurement geometry (see the supporting information). The geometric AMFs were within 20% of the model results for all elevation angles, and within 13% for elevation angles between 8 and 20° where the volcanic plume was located. We expect the associated errors of the retrieved H_2O VCD and SCDs presented in the following section to be $<$10% and therefore choose to adopt the geometrical approximation throughout this study, as has commonly been done by others in the past [e.g., *Hönninger et al.*, 2004; *Wagner et al.*, 2013].

One result of the geometric relationship is that the H_2O VCD equals the SCD detected while aimed at the zenith (see equation (2)). In other words, the light measured while pointing upward has passed through the vertical water vapor column exactly once, regardless of the solar zenith angle θ (see Figure 3). Though our scans unfortunately did not include an exact 90° measurement, equation (3) indicates that the light path of the 82° measurement was within 1% of the straight vertical column and can therefore be considered vertical for practical purposes.

Also, since the reference spectra contain absorption features associated with the VCD, the DSCDs that we obtain from our differential analyses of scanning spectra are actually representative of the difference between SCD and VCD

$$\mathrm{DSCD} = \mathrm{SCD} - \mathrm{VCD} = \mathrm{VCD}\,(\mathrm{AMF} - 1) \tag{4}$$

3.2. Saturation of Water Vapor Absorption Lines

Water vapor is different than most atmospheric trace gases that are commonly measured by DOAS in that instrument sensitivity is not usually an issue. The abundance of water vapor in the atmosphere and the relatively strong spectral absorption features throughout the visible and near-infrared spectral regions combine to produce large optical depths which are easily detected. The difficulties associated with these measurements instead stem from the fact that individual absorption lines are too narrow to be resolved by grating spectrometers deployed to the field or on satellite platforms. Figure 4 shows the absorption cross section of water vapor taken from the HITRAN2012 molecular spectroscopic database [*Rothman et al.*, 2013] between 713 and 748 nm. Convolution of this cross section with our Vis spectrometer's slit function yields our expected spectral response (red line in Figure 4) when measuring weak water vapor absorption [*Platt and Stutz*, 2008].

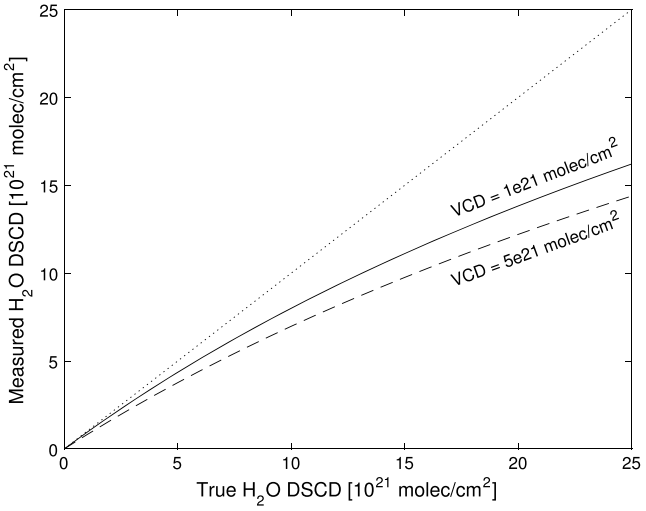

Figure 5. Modeled instrument response over the range of expected H_2O DSCDs. The nonlinearity of the instrument response stems from the inability of our spectrometer to resolve individual H_2O absorption lines. Since the zenith-pointing measurements contain the H_2O absorption associated with the atmospheric H_2O VCD, all measurements are relative to this value. The model results show that the H_2O VCD slightly influences the instrument response and two exemplary VCD scenarios are depicted here.

However, if the water vapor optical depth increases beyond about 0.1, the depth increase of individual water vapor absorption lines becomes nonlinear according to the Beer-Lambert-Bouguer law. This is sometimes called "saturation" of absorption lines. The result is that the low-resolution absorption spectrum measured by our spectrometer begins to change shape and the measured optical depth no longer scales linearly with the H_2O SCD. Since the maximum value of the H_2O absorption cross section in our selected wavelength interval is about 1×10^{-22} cm^2/molecule, this saturation threshold is attained if the measured H_2O SCD exceeds 1×10^{21} molecules/cm^2, a value which is almost 2 orders of magnitude below the average atmospheric H_2O VCD (see section 1.2).

For this reason, conventional DOAS measurements targeting the atmospheric H_2O VCD typically utilize the H_2O absorption bands at 590 or 650 nm [*Wagner et al.*, 2003, 2013] which are about an order of magnitude weaker than the 720 nm band we have selected. More recently, even weaker bands in the blue and UV spectral regions were explored [*Lampel et al.*, 2015]. But two factors led us to choose a stronger absorption band. For one, the water vapor VCD above our 5000 m measurement location is anticipated to be at least an order of magnitude lower than the atmospheric VCD at sea level. Second, our measurements are targeting a subtle increase in total atmospheric H_2O column caused by the volcanic plume rather than the total column itself. A stronger absorption band will provide greater sensitivity to that expectedly small enhancement.

Luckily, the effect of saturation on the spectrometer's sensitivity to water vapor SCD can be modeled relatively easily [*Wagner et al.*, 2003]. First, some value for the H_2O SCD is assumed. This SCD is then used to calculate a transmittance spectrum according to the Beer-Lambert-Bouguer law using the high-resolution absorption-cross section of H_2O. Next, this spectrum is convolved with our instrument slit function and down-sampled to the pixel resolution of our spectrometer. Finally, a DOAS fit is applied using the convolved H_2O cross section (red line in Figure 4) as a reference. Due to the saturation effect, the fit returns an SCD that is lower than the SCD assumed when generating the transmittance spectrum. This process can be repeated for various H_2O SCDs in the expected measurement range, thus characterizing the sensitivity of a given spectrometer to various true H_2O SCDs.

The characterization of our spectrometer for DOAS H_2O retrievals performed on the 720 nm absorption band is shown in Figure 5. The nonlinearity of the instrument response is clearly visible. Note that we have plotted the DSCD rather than the SCD here. Since we are not using a top-of-atmosphere reference, all of our differential measurements are relative to zenith-looking reference spectra. As per our discussion above, these already contain the absorption associated with the H_2O VCD over the instrument. Therefore, the described sensitivity study was performed multiple times using clear-sky reference spectra containing varying amounts of H_2O VCDs. Two examples are shown in Figure 5: H_2O VCD = 1×10^{21} molecules/cm^2 (solid line) and H_2O VCD = 5×10^{21} molecules/cm^2 (dashed line). After determining the actual H_2O VCD present during the scanning measurements (see section 4.1), the appropriate curve was used to correct all H_2O DSCD measurements presented in this study for the effect of line saturation.

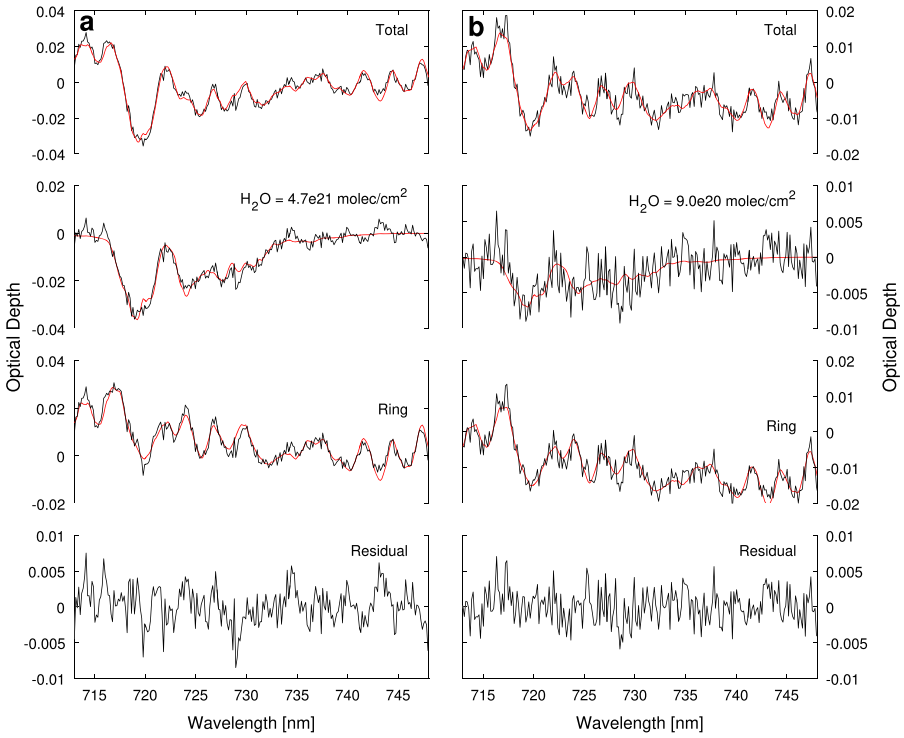

Figure 6. Spectral retrieval of H_2O between 713 and 748 nm. (a) Data collected during a scan of the Sabancaya plume. The DOAS fit yields an H_2O DSCD of 4.7×10^{21} molecules/cm^2. Applying the saturation correction yields 5.2×10^{21} molecules/cm^2. This column is 2.5×10^{21} molecules/cm^2 higher than the atmospheric column expected for plume-free conditions (see section 4). (b) Data collected during a vehicle traverse beneath the Sabancaya plume. The retrieved H_2O DSCD is 9.0×10^{20} molecules/cm^2 higher than the reference value measured after exiting from under the plume (compare Figure 11). Correction of the saturation effect yields an H_2O DSCD of 9.2×10^{20} molecules/cm^2.

3.3. Spectral Retrieval of Water Vapor

The DOAS retrieval of water vapor was performed in the same manner for both the scanning and the vehicle traverse measurements. The spectral range between 713 and 748 nm was chosen for the retrieval. The preprocessing and correction of spectra were analogous to the procedure described for the SO_2 analysis (section 2.4). The fit parameters used in the DOAS evaluation are summarized in Table 1.

Figure 6 depicts two example DOAS fits for a scanning measurement (Figure 6a) and for a traverse measurement (Figure 6b). In both cases, the result of the DOAS fit (red, top) appears to explain the measurements well (black, top) as is evidenced by the relatively small fit residual. Water vapor was detected in both of the two measurement spectra. Since the scanning spectrum shown in Figure 6a was recorded at an elevation angle α of 19° and evaluated against a zenith-looking reference, it is not surprising that a positive water vapor DSCD was retrieved, and at least part of it must stem from the atmospheric H_2O background. The retrieved value of 4.7×10^{21} molecules/cm^2 corresponds to 5.2×10^{21} molecules/cm^2 after saturation correction (see section 3.2). As will be shown later on, this is about twice as high as the expected atmospheric background DSCD at that elevation angle due to the presence of additional water vapor inside the Sabancaya plume. The retrieval shown in Figure 6b resulted in an H_2O DSCD of 9.0×10^{20} molecules/cm^2. Saturation correction yielded 9.2×10^{20} molecules/cm^2. Since this spectrum was recorded in zenith-looking direction while passing under the volcanic plume and evaluated relative to a zenith-looking clear-sky spectrum, this DSCD is actually a direct measurement of the enhancement in H_2O VCD by the volcanic plume (see section 4.3).

4. Water Vapor Measurement Results

In this section, we describe the results of our DOAS measurements of water vapor in the plume of Sabancaya Volcano. The measurements presented here were all recorded on 21 May 2016. Both upward looking traverse and scanning DOAS geometries were employed (see section 2 for details).

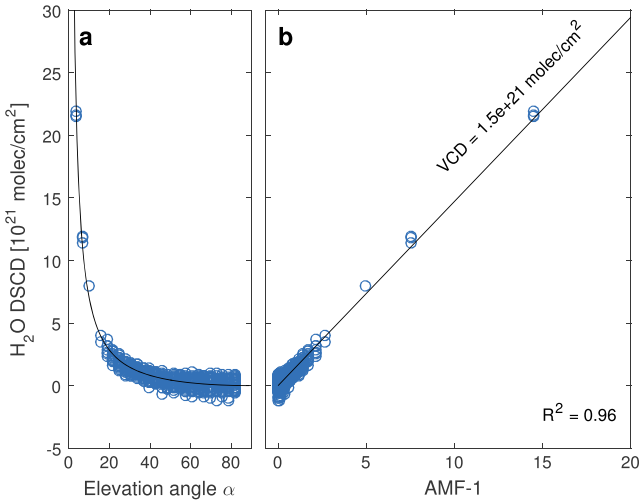

Figure 7. (a) When the H_2O DSCDs retrieved from all plume-free spectra during the measurement period are plotted against elevation angle α, they follow a clear 1/sin(α) trend (black line). (b) Plotting the same H_2O DSCDs against AMF-1, where AMF is the geometrical approximation for the air mass factor (equation (3)), yields the vertical column density (slope of black line, see text for derivation).

4.1. Atmospheric Water Vapor Column

As described in section 3.2, a correction must be applied to the H_2O DSCD values obtained from our DOAS fits to account for the influence of saturated H_2O absorption lines. This correction depends on the H_2O VCD present in our clear-sky reference spectra. Therefore, the first step in evaluating our spectral data is to determine the atmospheric H_2O VCD above our instrument at the time of the measurements.

For this purpose, the scanning UV measurements were first analyzed for SO_2. All Vis spectra for which the corresponding SO_2 column density was greater than 6×10^{17} molecules/cm^2 were initially filtered out. The remaining spectra can be considered largely uninfluenced by the volcanic plume and therefore representative of the atmospheric H_2O background. This is confirmed by the fact that the H_2O DSCDs retrieved from these spectra closely follow the trend expected for the geometric AMF. Figure 7 shows that the plume-free H_2O DSCDs are proportional to $1/\sin(\alpha) - 1$, as expected from equations (3) and (4). Plotting the DSCDs against AMF-1 yields a linear trend, the slope of which gives the H_2O VCD. A very high coefficient of determination $R^2 = 0.96$ was obtained, though it should be noted that the elevation angles initially associated with each scanner position had to be corrected by 4° to achieve this value. It is not surprising that the absolute determination of elevation angle was initially imperfect as no means for achieving absolute alignment of the scanner were available in the field.

A complicating factor in this determination of H_2O VCD stems from the need to correct the retrieved DSCDs for the saturation effect. Because this correction is itself dependent on the VCD (see section 3.2), a recursive method must be applied. An initial guess for the H_2O VCD is used to correct the clear-sky DSCDs for saturation. A new VCD is derived from the corrected DSCDs according to the method shown in Figure 7. This new H_2O VCD is then used for saturation correction in the next iteration. Starting with an a priori VCD of 1×10^{21} molecules/cm^2, we found that only two iterations were needed to constrain the atmospheric H_2O VCD to within 10% which is sufficiently precise for use in the saturation correction (see Figure 5). Using this method, we determined that the atmospheric H_2O VCD above our measurement location was $(1.5 \pm 0.1) \times 10^{21}$ molecules/cm^2.

4.2. Testing for Scattering on Plume Aerosols

After establishing that the background water vapor profile did indeed closely follow the expected trends for our radiative transfer assumptions, we checked for one other potential pitfall. Though the plume was clearly optically thin in the visible spectral range at the location of the scanning plane (Figure 2), there is still a potential for some amount of scattering to occur on aerosols within the plume. If the contribution of radiation scattered in the plume to our measurement spectra is significant, the geometrical approximation of AMF would no longer be valid for the in-plume measurements. As depicted by path C in Figure 3, this is due to the fact that the plume was located within the proximal atmospheric water vapor layer. Scattering of visible radiation on aerosols in the plume would therefore change the effective path length in this layer, thus affecting the measured water vapor DSCD without the need for an H_2O enhancement (or deficit) within the plume. In our particular case, the most likely effect would be a reduction in near-surface light path length, as the

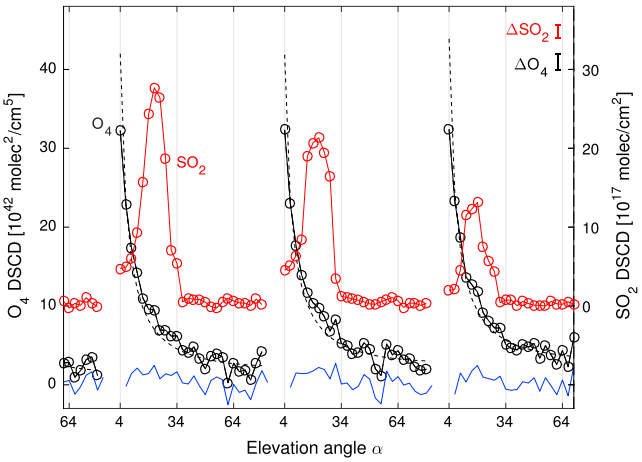

Figure 8. Three exemplary scans through the Sabancaya plume collected on 21 May 2016 between 14:54 and 15:11 local time. For each scan, the elevation angle α was stepped from 4 to 82° in increments of 3°. The SO_2 differential column density was retrieved from spectra collected with a UV spectrometer. It is depicted in red and shows the location of the volcanic gas plume in each scan. The black points represent the retrieved O_4 differential column density. The mean errors for SO_2 and O_4 are shown at top right. There is no systematic deviation from the 1/sin(α) trend expected for the geometrical air mass factor (dotted black line, difference shown in blue). Therefore, we find no evidence of the plume significantly affecting the light path distribution of incident radiation in the red spectral region.

plume was located at elevation angles α smaller than the solar elevation angle (90 − θ) during the measurement timeframe. To test for aerosol scattering, a DOAS analysis of O_4 was performed on the Vis spectra. O_4 is shorthand for the $(O_2)_2$ collision complex. Atmospheric O_4 forms when two oxygen molecules collide, and thus, its vertical concentration profile is proportional to the square of the oxygen profile and has an ~4 km scale height. DOAS measurements of O_4 are commonly used as a source of additional information on atmospheric radiative transfer [*Wagner et al.*, 2002, 2004; *Frieß et al.*, 2006]. The idea is that since the concentration profile is known, measured O_4 DSCDs are actually indicative of the radiative transfer between the Sun and the instrument rather than variations in the O_4 concentration.

We evaluated our measured spectra for O_4 absorption in the 560–610 nm spectral region. The details of the DOAS analysis are listed in Table 1. Figure 8 shows three exemplary scans through the Sabancaya plume measured between 14:50 and 15:06 local time on 21 May 2016. Plotted in red, the retrieved SO_2 DSCD clearly shows that the plume center was located at approximately 20° elevation during this period. The plume width was about 15° which, at the plume distance of 3.4 km, corresponds to about 900 m. In the plume center, SO_2 DSCDs of up to 2.8×10^{18} molecules/cm^2 were obtained. Assuming a circular plume cross section, this corresponds to an average SO_2 concentration of about 3×10^{13} molecules/cm^3.

The black points in Figure 8 depict the retrieved O_4 DSCDs from the same plume scans. According to equation (3), a 1/sin(α) trend should describe the O_4 DSCDs well as long as the geometric approximation for AMF holds true. This progression was fit to the O_4 DSCDs obtained in each of the scans. Elevation angles within the main bounds of the plume, i.e., with more than 6×10^{17} molecules/cm^2 SO_2, were not included in the fit. The fit results (shown as dotted black lines in Figure 8) generally describe the DSCDs well, with no systematic deviation from the expected atmospheric background trend visible at the location of the volcanic plume. In particular, there is no apparent dip in O_4 DSCDs at the plume location which is what we might expect if scattering of visible radiation on plume aerosols was occurring. Therefore, we find no evidence for a significant impact of plume aerosols on the radiative transfer of our scene in the red spectral region.

4.3. Water Vapor in the Sabancaya Plume

Since plume aerosols do not appear to be affecting radiative transfer, any enhancement of H_2O absorption over the atmospheric background found while scanning though the plume can be attributed to water vapor within the plume itself. Figure 9 shows the results of the water vapor DOAS retrieval, the details of which are described in section 3.3, for the same three exemplary scans shown in Figure 8. The SO_2 column density is again plotted in red, and the H_2O DSCD is now plotted in black. The atmospheric water vapor background is again expected to follow a 1/sin(α) relationship as per equation (3). As was previously done for O_4, this trend was fit to the H_2O DSCDs for each scan, again exempting H_2O values recorded within the main bounds of the plume ($SO_2 > 6 \times 10^{17}$ molecules/cm^2) from the fit.

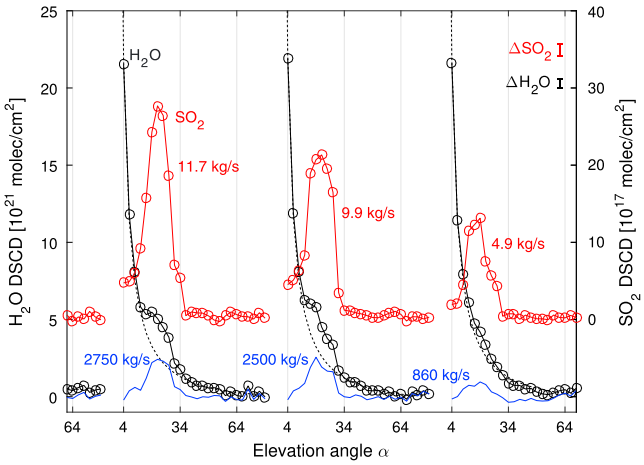

Figure 9. The black points depict H_2O DSCDs measured while scanning through the Sabancaya plume. All H_2O DSCDs have been corrected for the saturation effect. The SO_2 DSCDs measured in the UV spectral region are again shown in red for reference. The H_2O DSCDs show a systematic excess above the 1/sin(α) behavior expected for the background atmosphere (dotted black line) at the location of the volcanic gas plume. The difference between measured DSCD and expected atmospheric DSCD is shown in blue and reaches up to 2.6×10^{21} H_2O molecules/cm^2 in the plume center. Integration over the individual scans and multiplication by the 4.1 m/s wind speed yields the SO_2 and H_2O emission rates for each scan.

The H_2O DSCD trends expected for the background atmosphere are shown as dotted lines in Figure 9. The difference between our retrieved H_2O DSCDs and these trends is plotted in blue as a function of elevation angle. Here there does appear to be a significant systematic enhancement of the H_2O DSCDs over the atmospheric background at the exact location of the volcanic plume. This enhancement stems from light absorption by additional water vapor contained within the volcanic plume. The H_2O excess is significantly larger than the spectroscopic errors derived from the DOAS fit errors [*Stutz and Platt*, 1996], the mean values of which are shown in the top right corner of Figure 9. Up to $(2.7 \pm 0.4) \times 10^{21}$ molecules/cm^2 of excess water vapor was found when the scanner was aimed at the plume center. Again, assuming a circular plume cross section with a 900 m diameter, this corresponds to a concentration of about $(3.0 \pm 0.4) \times 10^{16}$ H_2O molecules/cm^3.

Integration across each of the three scans shown in Figure 9 yields the SO_2 and H_2O burden in the scanning plane. Multiplication of this burden with the 4.1 m/s wind speed gives a volcanic emission rate for each scan. The calculated emission rates for SO_2 and H_2O are noted next to each peak in Figure 9. The SO_2 emission rate declined from 11.7 kg/s to 4.9 kg/s during the depicted 15 min measurement interval. This change is greater than the estimated uncertainty of our measurements (~26%; see section 2.4). At the same time, the H_2O emission rate decreased from 2750 kg/s to 860 kg/s. The change in measured emissions may be caused by a short-term change in volcanic output, but the dynamics of the turbulent diffusion processes transporting the volcanic gas from the vent to the scanning plane are complex. Without detailed knowledge of the shape of the summit crater, the location of the main vent within it, and the locations of any additional fumaroles that may be contributing to the measured H_2O emissions, we cannot rule out the possibility that the measured drop in emissions was simply a result of turbulent atmospheric dispersion.

The accuracy and precision of these emission rates are mainly determined by (1) the accuracy and precision of the wind speed measurement and (2) the ability to accurately correct the measured DSCD for atmospheric water vapor. This atmospheric correction becomes increasingly sensitive to the accuracy of the elevation angle as the plume moves closer to the horizon because the correction term can become much larger than the plume-induced enhancement of the DSCD. We performed a sensitivity analysis by varying the elevation angle of each measurement by ±0.5°. We estimate this to be our angular precision based on the fact that larger variations significantly reduce the quality of the linear fit to the clear-sky DSCDs shown in Figure 7. For the scans shown here, a half degree uncertainty in elevation angle is on average associated with an ±27% error in the H_2O emission rates. Combined with the independent 20% relative error of the wind speed, we estimate the errors of each of the H_2O emission rates shown in Figure 9 and determined from individual scans to be ±35%. More accurate measurements would be possible if the plume were intersected at higher elevation angles, but unfortunately, our measurement geometry did not allow for that, and the depicted scans are examples taken from a time when the plume was intersected relatively high above the horizon compared to some of the other scans.

In an alternate approach, the H_2O emission rate can be derived by multiplying the measured H_2O/SO_2 ratio with the SO_2 emission rate. The blue circles in Figure 10 depict the excess H_2O DSCDs retrieved from all 24

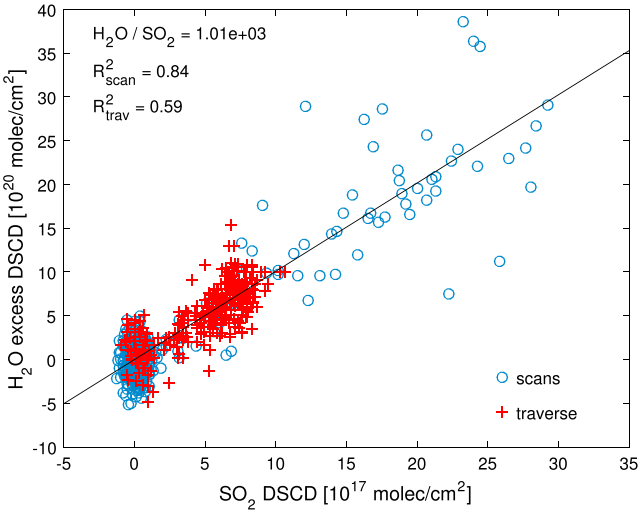

Figure 10. The excess H_2O DSCDs above the atmospheric background retrieved from plume scans (blue circles) and traverse measurements (red crosses) performed at Sabancaya volcano on 21 May 2016 are correlated with the SO_2 DSCDs retrieved from simultaneously recorded UV spectra. Both measurements found a molecular ratio of H_2O to SO_2 of 1.01×10^3 in the volcanic plume (black line).

plume scans recorded between 14:11 and 16:11 local time plotted against the SO_2 DSCDs measured coincidentally. For this plot, all data recorded at elevation angles of less than 15° have been removed. The data are thus limited to measurements in which the plume excess H_2O DSCD is at least comparable to the atmospheric background DSCD, thereby reducing the uncertainty related to the atmospheric corrections. Fitting a linear trend to these data yields a molecular H_2O/SO_2 ratio of 1.0×10^3. In other words, water vapor was found to be 1000 times more abundant than SO_2 in the plume. The coefficient of determination was 0.83, and the standard error of the slope was ±20% based on the standard deviation of individual DSCDs from the best fit. The calculated H_2O/SO_2 ratio is thus expected to be accurate to within ±20%, and our SO_2 emission rate measurements, for which no atmospheric corrections are needed, can now be scaled by this ratio. We thus obtain an H_2O emission rate of (2900 ± 870) kg/s or (250,000 ± 75,000) t/d from our scanning measurements.

The vehicle traverse measurements mentioned in section 2.2 were also analyzed for water vapor absorption. Interpretation of these measurements is simpler, as all spectra were recorded in zenith-looking direction. Therefore, the DSCDs retrieved relative to the zenith-pointing, clear-sky reference already represent the excess H_2O associated with the volcanic plume, and no further atmospheric correction is needed. However, note that determination of the atmospheric H_2O VCD, as was described in section 4.1, is still necessary in order to properly perform the saturation correction of the DOAS fit results (section 3.2).

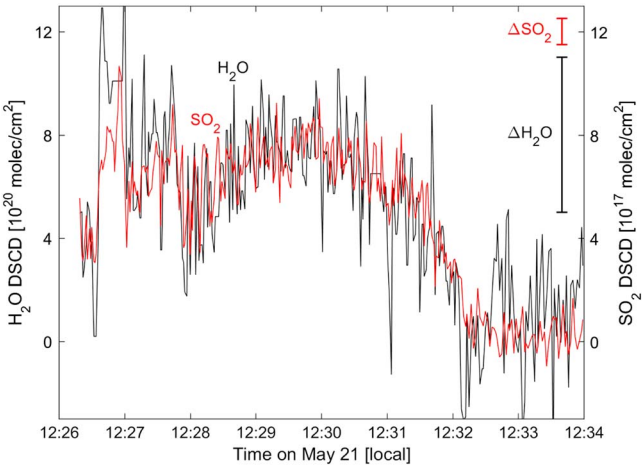

Figure 11. H_2O and SO_2 DSCDs retrieved from upward looking plume traverse measurements in the visible and UV spectral regions. The 300 spectra recorded while passing under the highest SO_2 column densities and then exiting out from under the plume are shown. H_2O and SO_2 are clearly correlated (also see Figure 10). The mean measurement errors derived from the DOAS fits are represented in the top right corner.

Figure 11 shows the H_2O and SO_2 DSCDs retrieved from spectra recorded while passing under the highest SO_2 burden and then exiting out from under the plume. The DSCD progression for both species is well correlated, though the relative measurement errors are larger here due to (1) the shorter 1 s integration time used during the traverse and (2) the lower absolute DSCDs associated with greater distance from the vent. The results of this measurement are plotted as red crosses in Figure 10. The larger errors and lower dynamic range yield a lower coefficient of determination for the linear regression, but the

retrieved H_2O/SO_2 ratio of 1.0×10^3 is exactly the same as that obtained from the scans. Multiplication with the 800 t/d SO_2 emission rate retrieved for the traverse yields an H_2O emission rate of (225,000 ± 68,000) t/d, which is well within the range of values obtained from the scanning measurements.

4.4. Potential Sources for Additional Error

The H_2O emission rate from Sabancaya Volcano is larger than one might expect based on volcanic gas compositions reported in the literature (see next section). Before interpreting these results, a few additional potential error sources should be discussed.

One relatively obvious potential error source is the effect of condensation in the plume. Besides affecting the atmospheric light path of radiation that reaches the instrument (see section 4.2), any H_2O present in the condensed, liquid, or solid phase would be invisible to our spectroscopic approach. A simple, back-of-the-envelope calculation can shed some light onto the significance of condensation in the Sabancaya plume. If we assume that the plume was well mixed with the atmospheric background in the scanning plane of the measurements, the absolute humidity inside the plume can be obtained by adding the plume and background water vapor concentrations. Our scanning measurements yielded an atmospheric background H_2O VCD of 1.5×10^{21} molecules/cm^2 over our instrument (see section 4.1). Taking into account the ~2 km scale height of H_2O in the atmosphere, this corresponds to an atmospheric water vapor concentration at the plume's altitude of about 5×10^{15} molecules/cm^3. Adding this to the enhanced H_2O concentration emitted from the volcano (~3×10^{16} molecules/cm^3; section 4.3) yields an absolute humidity of about 3.5×10^{16} H_2O molecules/cm^3 (~1 g/m^3) within the plume. This concentration is equivalent to an H_2O partial pressure of about 1.3 hPa.

For a given temperature, the H_2O saturation vapor pressure can be easily and quite accurately approximated using the August-Roche-Magnus formula [*August*, 1828; *Alduchov and Eskridge*, 1996]. During our measurements, the ambient temperature is estimated to have been between 5 and 10°C (based on the vehicle's thermometer). The temperature at plume height was likely several °C cooler, between about −5 and 0°C. This puts the in-plume H_2O saturation vapor pressure between about 4 and 6 hPa. Our measured water vapor concentration therefore corresponds to a relative humidity in the range of about 20–35%. Condensation is not efficient at such low relative humidity, which explains the relative transparency of the plume in the scanning plane. Despite the substantial H_2O output, we therefore expect the fraction of the H_2O present in the condensed phase and invisible to our measurements to have been negligible, though this will clearly not be the case for less favorable conditions [see *Matsushima and Shinohara*, 2006] (section 5.2).

Another potential error source comes from the need for an accurate correction of the atmospheric background. In our background correction, we implicitly assumed an atmospheric H_2O concentration profile that varies only with altitude and is otherwise homogeneous on the scale of our measurements. In principle, it is possible that a water-rich air parcel could be lofted to an altitude at which its H_2O concentration is higher than that of the surrounding air, thus giving the appearance of a water vapor plume. We see no evidence for this in our data, and it is unlikely to have influenced our measurements. For one, such "false" plumes would equilibrate relatively quickly with surrounding air, particularly in an environment as dry as that found at Sabancaya. Also, our background atmospheric measurements followed the geometric AMF approximation very closely, only deviating from the expected profile exactly at the location of the volcanic SO_2 plume.

Another explanation for a water vapor plume around Sabancaya Volcano could come from the presence of snow and ice around its summit. Sublimation of ice and snow is known to introduce water vapor into air passing over frozen terrain. Interestingly, though dry air does favor sublimation processes, the main controls on sublimation rate are the wind speed and porosity of the snowpack, neither of which are expected to be unusually high in our case. *Reba et al.* [2012] report sublimation rates of less than 1 mm/d as typical for mountainous terrain. Even when considering several square kilometer of snow-covered area around Sabancaya's summit, this value yields a maximum of only a few thousand t/d of H_2O introduced into the atmosphere by sublimation, orders of magnitude less than we detected in the volcanic plume.

Finally, though spectroscopic measurements have the clear advantage of being contact free and thus avoid many of the problems faced when using in situ sampling techniques, there are some potential error sources associated with them as well. For one, the saturation correction (section 3.2) depends on the resolution of the

instrument. If the instrument line shape changed over time, e.g., due to a temperature drift, this could impact the spectrometer's sensitivity to H_2O absorption. However, this effect would only be on the order of a few percent. Also, it is difficult to assess the magnitude of stray light in the visible-light spectra as, in contrast to the UV measurements, there is no measured spectral region that is expected to stay completely dark. The effect of stray light would be a filling-in of absorption lines, thereby reducing the measured H_2O column densities. However, if this effect were significant, a systematic misfit of the H_2O band would appear as a function of the absolute radiance measured in a given spectrum. Such a misfit was not observed in our measurements, so stray light was likely insignificant.

5. Discussion

5.1. Implications for Activity at Sabancaya Volcano

In an environmental context, the 250,000 t/d H_2O emission rate from Sabancaya is fairly modest when compared to natural evaporation from open water. For example, evaporation rates from nearby Lake Titicaca are estimated to be around 5 mm/d [*Declaux et al.*, 2007] which when scaled with its surface area of 8560 km^2 makes for an atmospheric input more than an order of magnitude greater than Sabancaya's H_2O emission rate. Therefore, the volcanic H_2O emissions are not expected to have a significant environmental impact other than perhaps in direct proximity to the vent.

In the context of volcanic activity, however, the measured water vapor emissions from Sabancaya are extremely high. For example, *Aiuppa et al.* [2008] report the average H_2O emissions from Mount Etna, one of the most prodigiously degassing volcanoes in the world, to lie around 13,000 t/d. The measured H_2O/SO_2 molecular ratio of 1000 is also much higher than typical H_2O/S ratios measured in andesitic melt. *Giggenbach* [1996] reports volatile compositions with molar ratios between 60 and 330 measured in melt inclusions of various andesitic magmas, with a mean value of 160. There are several possible explanations for our observations. For one, it is possible that the magma from which the gases originate is at a critical depth and temperature such that H_2O dissolution is favored over that of S. The solubility of H_2O in a melt is given by a relatively simple relationship between its partial pressure and concentration in the melt [*Holloway and Blank*, 1994]. The SO_2 solubility is more complex and depends on pressure, temperature, magma composition, and oxygen fugacity [*Scaillet et al.*, 1998; *Oppenheimer et al.*, 2011]. This complicates the process of evaluating the expected gas composition without additional information about the source region. However, based on comparison with gas emissions from other volcanoes around the world, it is improbable that preferential degassing of H_2O alone is responsible for the observed high H_2O/SO_2 ratio.

Instead, the interaction of magmatic gases with hydrothermal fluids together with a boiling-off of meteoric water provides a more likely explanation for our observations. Due to the relatively long period of repose since the last explosive eruption at Sabancaya in 1990, the hydrothermal system harbored by the volcanic edifice is likely to have been completely reestablished prior to the current episode of unrest. Therefore, gases exsolved from magma at depth will need to pass through this system prior to emission into the atmosphere. While interacting with meteoric water in the hydrothermal system, sulfur-bearing gases can be scrubbed and removed from the bulk plume [*Symonds et al.*, 2001]. Sulfur that does pass through the hydrothermal system will be at least partially reduced to H_2S and thus become invisible to our measurements.

Scrubbing would increase the measured H_2O/SO_2 ratio in the downwind plume over that of the relative volatile composition in the degassing magma. However, the significant SO_2 emission rate (800–900 t/d) observed during our measurements indicates that the scrubbing of sulfur gases is unlikely to be the only explanation for the high H_2O/SO_2 ratio. Instead, we believe that our measurements captured the boiling-off of Sabancaya's hydrothermal system. As magma moves to shallower depths in the volcanic edifice and the thermal flux into the hydrothermal system increases, additional water can be added to the magmatic gas emissions through boiling-off of hydrothermal fluids.

The boiling of hydrothermal fluids is likely to occur not only directly at the location of the volcanic conduit, thus adding H_2O to the bulk plume emitted from the main vent, but also in other areas throughout the volcanic edifice. The boiling process would then release water vapor through the porous cone and into the atmosphere, where it would mix with the bulk plume prior to reaching our measurement scanning plane. Locally, this process would manifest itself in water-rich, sulfur-poor gases diffusively degassing

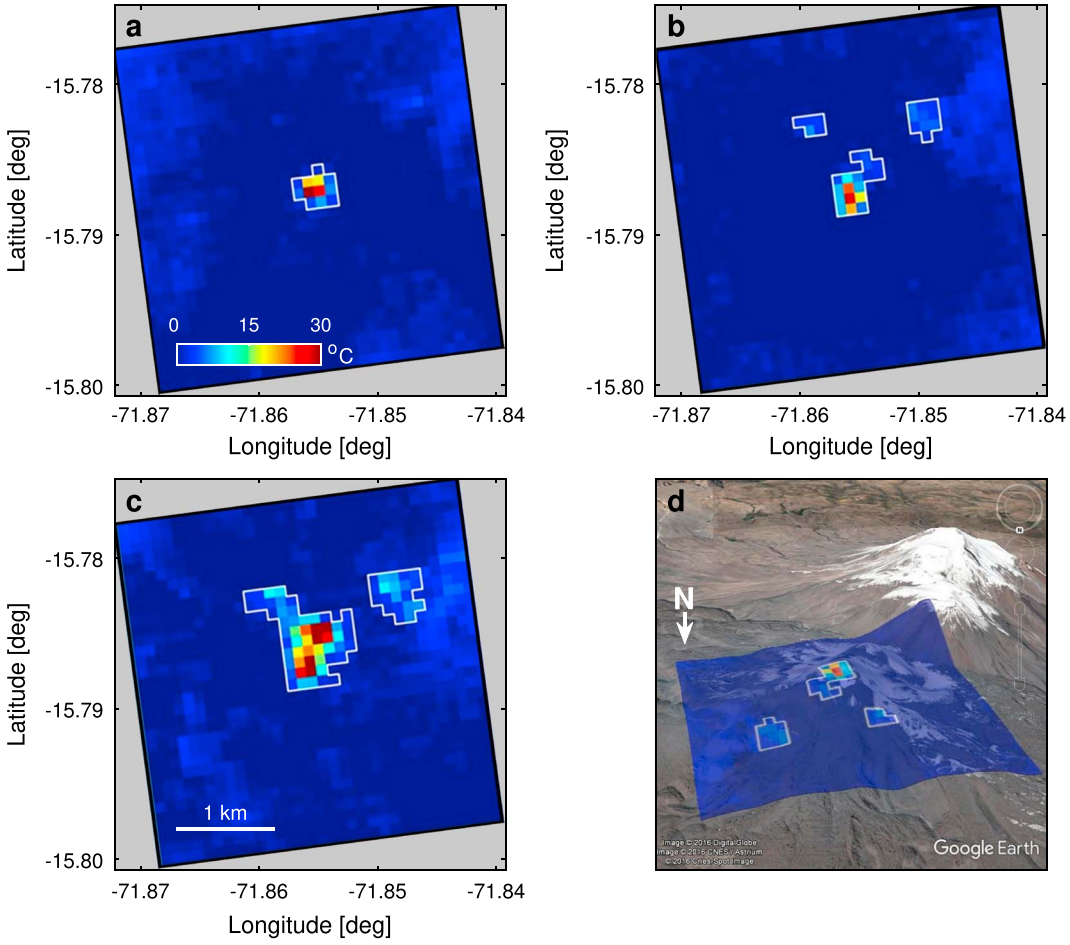

Figure 12. Thermal infrared (TIR) scene from ASTER acquired over the summit of Sabancaya Volcano on (a) 23 October 2015, 03:30:39 UTC; (b) 19 June 2016, 03:31:06 UTC; and (c) 3 November 2016, 03:24:16 UTC. Pixels exceeding 2°C above background have been outlined in white and are considered thermally anomalous. (d) An oblique view of the June 19 2016 TIR scene, as seen from the north, is overlaid on a satellite image and digital elevation model. Ampato Volcano is in the background. Three areas with anomalous temperatures away from the summit vent are clearly visible. The location of these areas coincides with locations at which fumaroles were observed to become visibly active shortly after our measurements in May 2016.

though soils and low-temperature (boiling point) fumaroles around the main high-temperature vent from which most of the SO_2 is emitted. The appearance of visibly steaming fumaroles observed away from the volcano's summit vent shortly after our measurements in May 2016 could be a manifestation of these processes. The relatively large short-term variability of the H_2O/SO_2 ratio observed at times during our measurement period also corroborates our hypothesis. For example, the H_2O/SO_2 ratio decreased by about 35% in only 15 min during the scans shown in Figure 9. Such short-term variability is consistent with heterogeneous mixing of gases with different compositions being emitted from spatially separate (but potentially overlapping) sources.

To provide some temporal context for our measurements, we analyzed thermal infrared (TIR) imagery from the Advanced Spaceborne Thermal Emission and Reflection Radiometer (ASTER) collected at Sabancaya before and after our measurement period. ASTER's TIR subsystem acquires pixels with a 90 m spatial resolution over five different channels within the spectral range of 8 to 12 μm [*Yamaguchi et al.*, 1998]. Figure 12 shows TIR scenes from October 2015, June 2016, and November 2016. For each image, level 2 atmospherically corrected surface-leaving radiance (AST_09T) [*Abrams*, 2000] was converted to temperature above background using an emissivity normalization approach wherein radiance data are separated into surface

emissivity and surface kinetic temperature [*Gillespie*, 1986]. The reported temperatures have an approximate radiometric accuracy of ±2°C [*Thome et al.*, 1998].

A thermal anomaly is identified as any pixel that has been elevated as the result of thermal activity [*Pieri and Abrams*, 2005; *Reath et al.*, 2016]. A background temperature was established from the average temperature of a 10 × 10 pixel area adjacent to the potentially active area but not included in the thermal anomalies. Due to the radiometric accuracy of these data, a 2°C threshold was established to identify thermally anomalous pixels within the potentially active area. This threshold was then applied to a region of interest containing all potential thermal anomalies, and the area of these anomalies was tracked over time. The total area increased consistently from 23 October 2015 until 3 November 2016, the last scene acquired before the eruption on 11 November 2016.

Figure 12 demonstrates the expansion of the thermal anomaly from 12 pixels on 23 October 2015, to 33 pixels on 19 June 2016, to 77 pixels on 3 November 2016. Starting with the June image (Figure 12b) and the corresponding oblique view (Figure 12d), three areas with anomalous temperatures outside the summit crater can be identified. These coincide with the location of visibly steaming fumaroles appearing around the same time and appear to grow in size and radiative output between June and November. Though the satellite-derived temperatures in the anomalous pixels range from 2 to 30°C above background, the actual temperatures were likely significantly higher, as the 90 m spatial resolution of the TIR sensor is insufficient to fully resolve these thermal features. Reported temperature values are thus obtained by averaging over both hot and cool areas. This also makes a quantitative analysis of the absolute thermal energy release difficult, but these data clearly point to an expansion and intensification of the thermal features over time. Presumably, as areas surrounding the summit heat up, hydrothermal fluids are boiled off, and hot volcanic gases are eventually able find new pathways through faults, cracks, and pore spaces. We believe our DOAS measurements captured the water vapor emissions associated with this preeruptive boiling.

5.2. Applicability of the Technique to Other Volcanoes

Though previously difficult to observe, it is likely that many volcanoes harboring hydrothermal systems experience periods of enhanced water vapor emissions prior to magmatic eruptions as hydrothermal fluids are boiled off. However, as we mentioned early on, the success of the DOAS measurements presented here was in part due to the very favorable conditions encountered at Sabancaya. Two important factors that led to the success of our measurements were (1) the relatively high H_2O emission rate at the time of the measurements and (2) the very high elevation of the volcano and, associated with this, the low atmospheric H_2O column above the instruments. Though these factors helped make our results particularly convincing, a few considerations can help determine how applicable our technique would be at other volcanoes with less ideal conditions.

The detection limit of DOAS systems is given by the shot statistics of the spectral radiance measurements themselves. A conservative estimate of the minimum detectable column density of a given absorbing trace gas can be obtained by assuming that for a positive detection, its measured optical depth must exceed the standard deviation of the overlaying noise by a factor of 2. In our case, the standard deviation of the measurement noise was about 2.5×10^{-3} (see residual plots in Figure 6) meaning that H_2O optical depths of $>5 \times 10^{-3}$ were detectable. Dividing this value by the amplitude of the convolved H_2O absorption cross section (~7.5×10^{-24} cm^2/molecule; see Figure 4) and correcting for the saturation effect (see section 3.2) yields a minimum detectable H_2O DSCD of about 7×10^{20} molecules/cm^2. Note that this is the detection limit for a single measurement spectrum. The H_2O DSCDs detected in our traverse measurement were not much higher than this limit, but the measurements become more and more convincing as an increasing number of spectra are recorded and an H_2O enhancement is detected in each.

Since our achieved detection limit was about 4 times below the maximum H_2O columns measured in the Sabancaya plume, we can estimate that the minimum detectable H_2O emission rate would have been about 700 kg/s or 60,000 t/d for the specific geometry and conditions of our measurements. In the same measurement conditions, a volcano emitting a pure, high-temperature magmatic gas with a typical H_2O/SO_2 ratio of 160 [*Giggenbach*, 1996] would need to emit about 1300 t/d of SO_2 to have a detectable, volcanogenic water vapor plume. This is not an uncommon SO_2 emission rate for active, open-vent volcanic systems, so it is likely that using our method, water vapor could be detected in

volcanic plumes even if no additional meteoric water were entrained, though the measurement conditions would have to be close to ideal.

The more problematic limitation of the DOAS technique for measuring volcanic H_2O output is associated with the relatively high atmospheric H_2O background. Clearly, the high elevation of our measurement site will not be achievable at most active volcanoes. When going to lower elevations, the accuracy of the atmospheric background correction will gain in importance. As long as the geometric approximation for the AMF holds, the technique will work. However, even slight deviations from the geometric approximation can potentially cause relatively large errors for plumes at lower altitudes.

The greatest potential source of error comes from the fact that a fraction of the measured light may have been scattered in the plume. Most large volcanic plumes will contain some amount of aerosols on which light can be scattered. When analyzed relative to a zenith-looking plume-free spectrum, the measured H_2O $DSCD_{meas}$ would then be given by the sum of the plume H_2O $DSCD_{plume}$ and an additional contribution from the atmosphere above the plume $DSCD_{atm}$. If we assume a volcanic plume directly above our instrument and a simple, single-scattering model for atmospheric radiative transfer, then any light that is scattered in the plume would have an additional path in the atmosphere that is inversely proportional to the cosine of the solar zenith angle θ (path C in Figure 3).

$$\mathrm{DSCD_{meas}} = \mathrm{DSCD_{plume}} + \mathrm{DSCD_{atm}} = \mathrm{DSCD_{plume}} + f \cdot \mathrm{VCD}(h) \cdot \left(\frac{1}{\cos(\theta)} - 1 \right) \tag{5}$$

Here f is the fraction of detected light (between 0 and 1) that was scattered in the plume and has therefore passed through the lower atmosphere at the solar zenith angle. Equation (5) shows that in addition to H_2O in the volcanic plume, atmospheric water vapor will contribute to the measured DSCD unless (1) aerosol scattering is negligible ($f \approx 0$) or (2) the Sun and the plume are straight overhead ($\theta \approx 0$) or (3) the H_2O VCD above the plume is negligible compared to the DSCD within the plume ($\mathrm{VCD}(h) \ll \mathrm{DSCD_{plume}}$). Our O_4 measurements and the transparent appearance of the Sabancaya plume indicate that aerosol scattering was negligible in our study, and for our 6 km plume height, we estimate VCD(h) to have been approximately 3 times smaller than $DSCD_{plume}$. Thus, for our measurements, $DSCD_{atm}$ can be neglected in equation (5).

However, this will not generally be the case. Clearly, DOAS measurements of H_2O will need to be limited to mostly transparent plumes. Measurements of opaque or condensing plumes with large aerosol optical depths will almost certainly be subject to large uncertainties induced by unknown radiative transfer. If we limit observations to plumes with $f < 0.1$ and require that the atmospheric contribution to the measured DSCD be less than 10% of the in-plume H_2O signal ($\mathrm{DSCD_{atm}} < 0.1 \cdot \mathrm{DSCD_{plume}}$), we find

$$\mathrm{VCD}(h) < \mathrm{DSCD_{plume}} \left(\frac{1}{\cos(\theta)} - 1 \right)^{-1} \tag{6}$$

For solar zenith angles θ of around 30°, this means that VCD(h) should not exceed ~6 times $DSCD_{plume}$. In a standard atmosphere, a plume comparable to that emitted from Sabancaya would thereby be accessible to DOAS measurements down to altitudes of approximately 3000 m. DOAS measurements of similar H_2O plumes emitted below that level would be subject to large uncertainties due to subtle variations in radiative transfer unless the parameters f, θ, and VCD(h) in equation (5) are all very well constrained. Less vigorous H_2O plumes will only be reliably measured at higher altitudes or smaller solar zenith angles, according to equation (6). Still, a significant number of active volcanoes emit plumes above 3 km altitude, and according to these admittedly rough estimates, our method should be applicable to these.

5.3. Potential Use of Water Vapor Measurements as a Forecasting Tool

Though only applicable to a subset of the world's most active volcanoes, DOAS measurements of water vapor could potentially provide valuable information for eruption forecasting. The measurements do suffer from ambivalence introduced by the likely interaction of volcanogenic volatiles with meteoric water, but this is a known issue and is not limited to H_2O/SO_2 ratios alone. Recent studies have shown that geochemical

measurements can provide eruption precursors despite, or even because of the varying degrees of interaction of magmatic gas with a hydrothermal system or volcanic lake [*de Moor et al.*, 2016a, 2016b]. The DOAS technique described in this study could offer continuous, reliable measurements of volcanic water vapor output that when interpreted in the context of other processes occurring at a given active volcano could provide volcano observatories with valuable information on the stage of activity.

To date, geochemical information used in eruption forecasts has largely been limited to compositional plume data (CO_2, SO_2, H_2S, and H_2O) measured by MultiGAS or similar instrumentation [*Aiuppa et al.*, 2007; *Werner et al.*, 2013; *de Moor et al.*, 2016a] and SO_2 emission rate data obtained from scanning DOAS measurements [e.g., *Olmos et al.*, 2007]. Recent findings suggest that the abundance of bromine monoxide (BrO) and chlorine dioxide (OClO) in high-temperature volcanic gases might also be sensitive to shallow magmatic recharge [*Bobrowski and Giuffrida*, 2012; *Lübcke et al.*, 2013], which is interesting mainly due to our ability to measure these species with scanning DOAS.

However, with the notable exception of CO_2, all of these parameters suffer from the difficulties involved with interaction of magmatic gases with volcanic hydrothermal systems. Sulfur and halogen species are particularly soluble in water and hydrothermal fluids, and thus, emissions associated with shallow magmatic recharge can easily be masked by scrubbing processes unless a relatively dry pathway exists for gases to escape. Such dry pathways often exist at volcanoes with persistent high-temperature degassing activity but are unlikely to exist in the initial phase of reactivation at long-dormant volcanoes.

Water vapor emissions, on the other hand, may provide valuable information about shallow magmatic recharge in wet volcanic systems. As magma is intruded to shallow depths, the associated thermal input will generally cause hydrothermal systems to boil off. If the evaporated water cannot easily escape, then pressure can build and culminate in phreatic explosions. On the other hand, more permeable systems will allow water vapor to escape effusively. In such systems, large pulses of water vapor emission could precede the first magmatic eruptions, as the hydrothermal fluids are boiled off. In fact, such water vapor exhalations might easily precede changes in most other geochemical parameters. In our case, for example, high H_2O emissions were detected months before the SO_2 emissions had reached their maximum preeruptive values (~6000 t/d). Elevated CO_2 emissions might provide more advanced warning, but currently CO_2 can only be monitored in a continuous manner by placing instruments directly at the suspected source location of future degassing. Visible-light DOAS measurements, on the other hand, could be implemented at high-altitude volcanoes with relative ease, for example by collocating visible spectrometers with existing scanning DOAS infrastructure. At volcanoes harboring hydrothermal systems, visible-light DOAS measurements could thus provide a new, largely independent geochemical parameter that when used in combination with complimentary geophysical information could help improve eruption forecasts.

6. Conclusions

In this study, we first describe a novel method for measuring volcanic H_2O emissions. These are the first measurements of volcanic water vapor using the DOAS remote sensing technique and, to our knowledge, the first direct measurements of water vapor emission rates from a passively degassing volcano. We find that the main difficulty in passive remote sensing of volcanic water vapor is performing a sufficiently accurate correction of the atmospheric background H_2O column. As discussed in section 5.2, the keys to successful measurements are (1) avoiding plumes with scattering aerosols and/or condensed water droplets, (2) performing measurements at high elevations to minimize the overhead background water vapor column, and (3) limiting measurements to low solar zenith angles around solar noon.

Our measurements at Sabancaya volcano yielded interesting and unprecedented results. The favorable timing of our experiment and nearly ideal measurement conditions allowed us to detect an extremely high preeruptive H_2O emission rate 6 months prior to the first explosive activity at Sabancaya during its current eruptive crisis. As the detected H_2O/SO_2 ratio is much higher than expected from the relative composition of these species in the magma, we believe that the large H_2O emissions stem from the boiling-off of Sabancaya's shallow hydrothermal system. This hypothesis is corroborated by the coincident appearance of fumaroles and anomalous thermal features around the volcano's main summit crater (section 5.1). We speculate that similarly high preeruptive water vapor emissions are likely to occur at other "wet" volcanoes

harboring significant hydrothermal systems and that visible-light DOAS monitoring could help identify these events and thus inform eruption forecasts.

Acknowledgments
The authors would like to thank OVI-INGEMMET staff for the support provided in field operations. The measurements shown here were recorded on one of many days spent in the field together, at times working under quite harsh conditions. Thanks also to Peter Kelly, Cynthia Werner, and Terry Gerlach for their fruitful discussions on the somewhat surprising results we obtained. We are very grateful for the thoughtful reviews by Andrew McGonigle, Jennifer Lewicki, and one anonymous reviewer which greatly improved this study. The USAID Office of Foreign Disaster Assistance is gratefully acknowledged for their support of our work in Peru. All DOAS spectral data collected at Sabancaya Volcano and evaluated and interpreted as part of this study are available for download from the USGS ScienceBase-Catalog [*Kern et al.*, 2017]. ASTER L2_TIR data can be accessed and ordered through the USGS Global Visualization Viewer (GloVis) website. https://glovis.usgs.gov/. Any used of trade, firm, or product names is for descriptive purposes only and does not imply endorsement by the U.S. Government.

References

Abrams, M. (2000), The Advanced Spaceborne Thermal Emission and Reflection Radiometer (ASTER): Data products for the high spatial resolution imager on NASA's Terra platform, *Int. J. Remote Sens.*, *21*(5), 847–859, doi:10.1080/014311600210326.

Aiuppa, A., R. Moretti, C. Federico, G. Giudice, S. Gurrieri, M. Liuzzo, P. Papale, H. Shinohara, and M. Valenza (2007), Forecasting Etna eruptions by real-time observation of volcanic gas composition, *Geology*, *35*(12), 1115–1118, doi:10.1130/G24149A.1.

Aiuppa, A., G. Giudice, S. Gurrieri, M. Liuzzo, M. Burton, T. Caltabiano, A. J. S. McGonigle, G. Salerno, H. Shinohara, and M. Valenza (2008), Total volatile flux from Mount Etna, *Geophys. Res. Lett.*, *35*, L24302, doi:10.1029/2008GL035871.

Alduchov, O. A., and R. E. Eskridge (1996), Improved Magnus form approximation of saturation vapor pressure, *J. Appl. Meteorol.*, *35*(4), 601–609, doi:10.1175/1520-0450(1996)035<0601:IMFAOS>2.0.CO;2.

August, E. F. (1828), Ueber die Berechnung der Expansivkraft des Wasserdunstes, *Ann. Phys.*, *89*, 122–137, doi:10.1002/andp.18280890511.

Beirle, S., H. Sihler, and T. Wagner (2013), Linearisation of the effects of spectral shift and stretch in DOAS analysis, *Atmos. Meas. Tech.*, *6*(3), 661–675, doi:10.5194/amt-6-661-2013.

Blake, S. (1984), Volatile oversaturation during the evolution of silicic magma chambers as an eruption trigger, *J. Geophys. Res.*, *89*(B10), 8237–8244, doi:10.1029/JB089iB10p08237.

Bobrowski, N., and G. Giuffrida (2012), Bromine monoxide/sulphur dioxide ratios in relation to volcanological observations at Mt. Etna 2006–2009, *Solid Earth*, *3*(2), 433–445, doi:10.5194/se-3-433-2012.

Bogumil, K., et al. (2003), Measurements of molecular absorption spectra with the SCIAMACHY pre-flight model: Instrument characterization and reference data for atmospheric remote-sensing in the 230–2380 nm region, *J. Photochem. Photobiol. A Chem.*, *157*(2–3), 167–184, doi:10.1016/S1010-6030(03)00062-5.

Botcharnikov, R. E., K. I. Shmulovich, S. I. Tkachenko, M. A. Korzhinsky, and A. V. Rybin (2003), Hydrogen isotope geochemistry and heat balance of a fumarolic system: Kudriavy volcano, Kuriles, *J. Volcanol. Geotherm. Res.*, *124*(1–2), 45–66, doi:10.1016/S0377-0273(03)00043-X.

Bower, S. M., and A. W. Woods (1997), Control of magma volatile content and chamber depth on the mass erupted during explosive volcanic eruptions, *J. Geophys. Res.*, *102*(B5), 10,273–10,290, doi:10.1029/96JB03176.

Burton, M. R., C. M. Oppenheimer, L. A. Horrocks, and P. W. Francis (2000), Remote sensing of CO2 and H2O emission rates from Masaya volcano, Nicaragua, *Geology*, *28*(10), 915–918.

Cahen, C., G. Mégie, and P. Flamant (1982), Lidar monitoring of the water vapor cycle in the troposphere, *J. Appl. Meteorol.*, *21*, 1506–1515.

Carey, S., and H. Sigurdsson (1989), The intensity of plinian eruptions, *Bull. Volcanol.*, *51*(1), 28–40, doi:10.1007/BF01086759.

Committee for the Extension of the U.S. Standard Atmosphere (1976), *U.S. Standard Atmosphere, United States Committee on Extension to the Standard Atmosphere*, 241 pp., U.S. Gov. Print. Off., Washington, D. C.

Declaux, F., A. Coudrain, and T. Condom (2007), Evaporation estimation on Lake Titicaca: A synthesis review and modelling, *Hydrol. Process.*, *21*, 1664–1677, doi:10.1002/hyp.6360.

Deutschmann, T., et al. (2011), The Monte Carlo atmospheric radiative transfer model McArtim: Introduction and validation of Jacobians and 3D features, *J. Quant. Spectrosc. Radiat. Transf.*, *112*(6), 1119–1137, doi:10.1016/j.jqsrt.2010.12.009.

de Moor, J. M., A. Aiuppa, J. Pacheco, G. Avard, C. Kern, M. Liuzzo, M. Martínez, G. Giudice, and T. P. Fischer (2016a), Short-period volcanic gas precursors to phreatic eruptions: Insights from Poás volcano, Costa Rica, *Earth Planet. Sci. Lett.*, *1*, 218–227, doi:10.1016/j.epsl.2016.02.056.

de Moor, J. M., et al. (2016b), Turmoil at Turrialba volcano (Costa Rica): Degassing and eruptive processes inferred from high-frequency gas monitoring, *J. Geophys. Res. Solid Earth*, *121*, 5761–5775, doi:10.1002/2016JB013150.

de Silva, S. L., and P. W. Francis (1990), Potentially active volcanoes of Peru - observations using Landsat Thematic Mapper and Space Shuttle imagery, *Bull. Volcanol.*, *52*, 286–301, doi:10.1007/BF00304100.

de Silva, S. L., and P. Francis (1991), *Volcanoes of the Central Andes*, 216 pp., Springer, Berlin.

Frieß, U., P. S. Monks, J. J. Remedios, A. Rozanov, R. Sinreich, T. Wagner, and U. Platt (2006), MAX-DOAS O4 measurements: A new technique to derive information on atmospheric aerosols: 2. Modeling studies, *J. Geophys. Res.*, *111*, D14203, doi:10.1029/2005JD006618.

Gaffen, D. J., A. Robock, and W. P. Elliott (1992), Annual cycles of tropospheric water vapor, *J. Geophys. Res.*, *97*(D16), 18,185–18,193, doi:10.1029/92JD01999.

Galle, B., C. Oppenheimer, A. Geyer, A. J. S. Mcgonigle, M. Edmonds, and L. Horrocks (2002), A miniaturised ultraviolet spectrometer for remote sensing of SO_2 fluxes: A new tool for volcano surveillance, *J. Volcanol. Geotherm. Res.*, *119*, 241–254.

Galle, B., M. Johansson, C. Rivera, Y. Zhang, M. Kihlman, C. Kern, T. Lehmann, U. Platt, S. Arellano, and S. Hidalgo (2010), Network for Observation of Volcanic and Atmospheric Change (NOVAC)—A global network for volcanic gas monitoring: Network layout and instrument description, *J. Geophys. Res.*, *115*, D05304, doi:10.1029/2009JD011823.

Gerbe, M. C., and J. C. Thouret (2004), Role of magma mixing in the petrogenesis of tephra erupted during the 1990–98 explosive activity of Nevado Sabancaya, southern Peru, *Bull. Volcanol.*, *66*(6), 541–561, doi:10.1007/s00445-004-0340-3.

Gerlach, T. M. (2004), Volcanic sources of tropospheric ozone-depleting trace gases, *Geochem. Geophys. Geosyst.*, *5*, Q09007, doi:10.1029/2004GC000747.

Giggenbach, W. F. (1996), Chemical composition of volcanic gases, in *Monitoring and Mitigation of Volcano Hazards*, edited by R. Scarpa and R. Tilling, pp. 221–256, Springer, Berlin.

Gillespie, A. R. (1986), Lithologic mapping of silicate rocks using TIMS, in *Jet Propulsion Laboratory Publication 86–38. The TIMS Data User's Workshop, June 18–19, 1985*, pp. 29–44, Pasadena, Calif. [Available at https://ntrs.nasa.gov/search.jsp?R=19870007685.]

Girona, T., F. Costa, B. Taisne, B. Aggangan, and I. Sorvigenaleon (2015), Fractal degassing from Erebus and Mayon volcanoes revealed by a new method to monitor H_2O emission cycles, *J. Geophys. Res. Solid Earth*, *120*, 2988–3002, doi:10.1002/2014JB011797.

Goff, F., and G. M. McMurtry (2000), Tritium and stable isotopes of magmatic waters, *J. Volcanol. Geotherm. Res.*, *97*(1–4), 347–396, doi:10.1016/S0377-0273(99)00177-8.

Grainger, J. F., and J. Ring (1962), Anomalous Fraunhofer line profiles, *Nature*, *193*, 762.

Hermans, C. (2010), Measurement of absorption cross sections and spectroscopic molecular parameters—O_2 and its collisonal induced absorption. [Available at http://spectrolab.aeronomie.be/o2.htm, (Accessed 17 November 2016).]

Herzog, M., H.-F. Graf, C. Textor, and J. M. Oberhuber (1998), The effect of phase changes of water on the development of volcanic plumes, *J. Volcanol. Geotherm. Res.*, *87*(1–4), 55–74, doi:10.1016/S0377-0273(98)00100-0.

Hinkley, T. K., J. E. Quick, R. T. Gregory, and T. M. Gerlach (1995), Hydrogen and oxygen isotopic compositions of waters from fumaroles at Kilauea summit, Hawaii, *Bull. Volcanol.*, *57*(1), 44–51, doi:10.1007/BF00298706.

Holloway, J. R., and J. G. Blank (1994), Application of experimental results to C-O-H species in natural melts, in *Volatiles in Magmas*, *Rev. Mineral.*, vol. 30, edited by M. R. Carroll and J. R. Holloway, pp. 187–230, Mineral. Soc. of Am., Washington, D. C.

Hönninger, G., C. von Friedeburg, and U. Platt (2004), Multi axis differential optical absorption spectroscopy, *Atmos. Chem. Phys.*, *4*, 231–254.

ITU (2012), Recommendation ITU-R P.835-5. Reference standard atmospheres, International Telecommunication Union.

Joshi, M. M., and G. S. Jones (2009), The climatic effects of the direct injection of water vapour into the stratosphere by large volcanic eruptions, *Atmos. Chem. Phys. Discuss.*, *9*(2), 6109–6118, doi:10.5194/acpd-9-5447-2009.

Joshi, M. M., and K. P. Shine (2003), A GCM study of volcanic eruptions as a cause of increased stratospheric water vapor, *J. Clim.*, *16*(21), 3525–3534, doi:10.1175/1520-0442(2003)016<3525:AGSOVE>2.0.CO;2.

Kern, C., T. Deutschmann, L. Vogel, M. Wöhrbach, T. Wagner, and U. Platt (2009), Radiative transfer corrections for accurate spectroscopic measurements of volcanic gas emissions, *Bull. Volcanol.*, *72*(2), 233–247, doi:10.1007/s00445-009-0313-7.

Kern, C., P. Masias, and F. Apaza (2017), Differential Optical Absorption Spectroscopy data acquired at Sabancaya Volcano (Peru) on 21 May 2016, *U.S. Geol. Surv. Data Release*, doi:10.5066/F7VH5M1B.

Kraus, S. (2006), DOASIS: A framework design for DOAS, Shaker.

Lampel, J., D. Pohler, J. Tschritter, U. Frieß, and U. Platt (2015), On the relative absorption strengths of water vapour in the blue wavelength range, *Atmos. Meas. Tech.*, *8*(10), 4329–4346, doi:10.5194/amt-8-4329-2015.

Löffler, M., S. Brinkop, and P. Jöckel (2016), Impact of major volcanic eruptions on stratospheric water vapour, *Atmos. Chem. Phys.*, *16*(10), 6547–6562, doi:10.5194/acp-16-6547-2016.

Love, S. P., F. Goff, S. C. Schmidt, C. Dale, B. W. Christenson, and C. Siebe (2000), Passive Infrared Spectroscopic Remote Sensing of Volcanic Gases: Ground-Based Studies at White Island and Ruapehu, New Zealand, and Popocatépetl, Mexico, in *Remote Sensing of Active Volcanism*, edited by P. J. Mouginis-Mark, J. A. Crisp and J. H. Fink, AGU, Washington, D. C., doi:10.1029/GM116p0117.

Lübcke, P., N. Bobrowski, S. Arellano, B. Galle, G. Garzón, L. Vogel, and U. Platt (2013), BrO/SO2 molar ratios from scanning DOAS measurements in the NOVAC network, *Solid Earth Discuss.*, *5*(2), 1845–1870, doi:10.5194/sed-5-1845-2013.

Matsushima, N., and H. Shinohara (2006), Visible and invisible volcanic plumes, *Geophys. Res. Lett.*, *33*, L24309, doi:10.1029/2006GL026506.

Maurellis, A. H., R. Lang, W. J. van der Zande, I. Aben, and W. Ubachs (2000), Precipitable water column retrieval from GOME data, *Geophys. Res. Lett.*, *27*(6), 903–906, doi:10.1029/1999GL010897.

Naughton, J. J., J. V. Derby, and R. B. Glover (1969), Infrared measurements on volcanic gas and fume: Kilauea eruption, 1968, *J. Geophys. Res.*, *74*(12), 3273–3277, doi:10.1029/JB074i012p03273.

Noël, S., M. Buchwitz, H. Bovensmann, R. Hoogen, and J. P. Burrows (1999), Atmospheric water vapor amounts retrieved from GOME satellite data, *Geophys. Res. Lett.*, *26*(13), 1841–1844, doi:10.1029/1999GL900437.

Noël, S., M. Buchwitz, and J. P. Burrows (2004), First retrieval of global water vapour column amounts from SCIAMACHY measurements, *Atmos. Chem. Phys.*, *4*(1), 111–125, doi:10.5194/acp-4-111-2004.

Olmos, R., et al. (2007), Anomalous emissions of SO_2 during the recent eruption of Santa Ana volcano, El Salvador, central America, *Pure Appl. Geophys.*, *164*(12), 2489–2506, doi:10.1007/s00024-007-0276-6.

Oppenheimer, C., and P. R. Kyle (2008), Probing the magma plumbing of Erebus Volcano, Antarctica, by open-path FTIR spectroscopy of gas emissions, *J. Volcanol. Geotherm. Res.*, *177*(3), 743–754, doi:10.1016/j.jvolgeores.2007.08.022.

Oppenheimer, C., B. Scaillet, and R. S. Martin (2011), Sulfur degassing from volcanoes: Source conditions, surveillance, plume chemistry and Earth system impacts, *Rev. Mineral. Geochem.*, *73*(1), 363–421, doi:10.2138/rmg.2011.73.13.

Palchetti, L., G. Bianchini, B. Carli, U. Cortesi, and S. Del Bianco (2007), Measurement of the water vapour vertical profile and of the Earth's outgoing far infrared flux, *Atmos. Chem. Phys. Discuss.*, *7*(6), 17,741–17,767, doi:10.5194/acpd-7-17741-2007.

Pering, T. D., A. J. S. Mcgonigle, G. Tamburello, A. Aiuppa, M. Bitetto, C. Rubino, and T. C. Wilkes (2017), A novel and inexpensive method for measuring volcanic plume water fluxes at high temporal resolution, *Remote Sens.*, *9*(146), 1–13, doi:10.3390/rs9020146.

Pieri, D., and M. Abrams (2005), ASTER observations of thermal anomalies preceding the April 2003 eruption of Chikurachki volcano, Kurile Islands, Russia, *Remote Sens. Environ.*, *99*(1), 84–94, doi:10.1016/j.rse.2005.06.012.

Platt, U., and J. Stutz (2008), *Differential Optical Absorption Spectroscopy - Principles and Applications*, 598 pp., Springer, Berlin.

Randel, D. L., T. H. Vonder Harr, M. A. Ringerud, G. L. Stephens, T. J. Greenwald, and C. L. Combs (1996), A new global water vapor dataset, *Bull. Am. Meteorol. Soc.*, *77*(6), 1233–1246.

Reath, K. A., M. S. Ramsey, J. Dehn, and P. W. Webley (2016), Predicting eruptions from precursory activity using remote sensing data hybridization, *J. Volcanol. Geotherm. Res.*, *321*, 18–30, doi:10.1016/j.jvolgeores.2016.04.027.

Reba, M. L., J. Pomeroy, D. Marks, and T. E. Link (2012), Estimating surface sublimation losses from snowpacks in a mountain catchment using eddy covariance and turbulent transfer calculations, *Hydrol. Process.*, *26*(24), 3699–3711, doi:10.1002/hyp.8372.

Rothman, L. S., et al. (2013), The HITRAN2012 molecular spectroscopic database, *J. Quant. Spectrosc. Radiat. Transf.*, *130*, 4–50, doi:10.1016/j.jqsrt.2013.07.002.

Samaniego, P., M. Rivera, J. Mariño, H. Guillou, C. Liorzou, S. Zerathe, R. Delgado, P. Valderrama, and V. Scao (2016), The eruptive chronology of the Ampato-Sabancaya volcanic complex (Southern Peru), *J. Volcanol. Geotherm. Res.*, *323*, 110–128, doi:10.1016/j.jvolgeores.2016.04.038.

Scaillet, B., B. Clemente, B. W. Evans, and M. Pichavant (1998), Redox control of sulfur degassing in silicic magmas, *J. Geophys. Res.*, *103*(B10), 23,937–23,949, doi:10.1029/98JB02301.

Sierk, B., S. Solomon, J. S. Daniel, R. W. Portmann, S. I. Gutman, A. O. Langford, C. S. Eubank, E. G. Dutton, and K. H. Holub (2004), Field measurements of water vapor continuum absorption in the visible and near-infrared, *J. Geophys. Res.*, *109*, D08307, doi:10.1029/2003JD003586.

Sioris, C. E., A. Malo, C. A. McLinden, and R. D'Amours (2016), Direct injection of water vapor into the stratosphere by volcanic eruptions, *Geophys. Res. Lett.*, *43*, 7694–7700, doi:10.1002/2016GL069918.

Soden, B. J., R. T. Wetherald, G. L. Stenchikov, and A. Robock (2002), Global cooling after the eruption of mount pinatubo: A test of climate feedback by water vapor, *Science*, *296*(5568), 727–730.

Solomon, S., K. H. Rosenlof, R. W. Portmann, J. S. Daniel, S. M. Davis, T. J. Sanford, and G.-K. Plattner (2010), Contributions of stratospheric water vapor to decadal changes in the rate of global warming, *Science*, *327*(5970), 1219–1223, doi:10.1126/science.1182488.

Sparks, R. S. J. (1978), The dynamics of bubble formation and growth in magmas: A review and analysis, *J. Volcanol. Geotherm. Res.*, *3*, 1–37, doi:10.1016/0377-0273(78)90002-1.

Stutz, J., and U. Platt (1996), Numerical analysis and estimation of the statistical error of differential optical absorption spectroscopy measurements with least-squares methods, *Appl. Opt.*, *35*(30), 6041–6053, doi:10.1364/AO.35.006041.

Symonds, R. B., W. I. Rose, T. M. Gerlach, P. H. Briggs, and R. S. Harmon (1990), Evaluation of gases, condensates, and SO2 emissions from Augustine volcano, Alaska: The degassing of a Cl-rich volcanic system, *Bull. Volcanol.*, *52*, 355–374.

Symonds, R. B., W. I. Rose, G. J. S. Bluth, and T. M. Gerlach (1994), Volcanic-gas studies: Methods, results, and applications, in *Volatiles in Magmas*, *Rev. Mineral.*, vol. 30, edited by M. R. Carroll and J. R. Hollaway, pp. 1–66, Miner. Soc. of Am., Chantilly, Va.

Symonds, R. B., T. M. Gerlach, and M. H. Reed (2001), Magmatic gas scrubbing: Implications for volcano monitoring, *J. Volcanol. Geotherm. Res.*, *108*, 303–341.

Textor, C., H. Graf, C. Timmreck, and A. Robock (2004), Emissions from volcanoes, in *Emissions of Atmospheric Trace Compounds*, edited by C. Granier, P. Artaxo, and C. Reeves, pp. 1–32, Springer, Berlin.

Thome, K., et al. (1998), ASTER preflight and inflight calibration and the validation of level 2 products, *IEEE Trans. Geosci. Remote Sens.*, *36*(4), 1161–1172.

Tomasi, C. (1984), Vertical distribution features of atmospheric water vapor in the Mediterranean, Red Sea and Indian Ocean, *J. Geophys. Res.*, *89*, 2563–2566, doi:10.1029/JD089iD02p02563.

Turner, D. D., R. A. Ferrare, and L. A. Brasseur (2001), Average aerosol extinction and water vapor profiles over the Southern Great Plains, *Geophys. Res. Lett.*, *28*(23), 4441–4444, doi:10.1029/2001GL013691.

USGS (2006), Shuttle Radar Topography mission, 3 arc second resolution, version 2.1. [Available at http://dds.cr.usgs.gov/srtm/version2_1/.]

Vandaele, A. C., C. Hermans, and S. Fally (2009), Fourier transform measurements of SO2 absorption cross sections: II. Temperature dependence in the 29 000–44 000 cm^{-1} (227–345 nm) region, *J. Quant. Spectrosc. Radiat. Transf.*, *110*(18), 2115–2126, doi:10.1016/j.jqsrt.2009.05.006.

Wagner, T., C. Von Friedeburg, M. Wenig, C. Otten, and U. Platt (2002), UV-visible observations of atmospheric O_4 absorptions using direct moonlight and zenith-scattered sunlight for clear-sky and cloudy sky conditions, *J. Geophys. Res.*, *107*(D20), 4424, doi:10.1029/2001JD001026.

Wagner, T., J. Heland, M. Zoger, and U. Platt (2003), A fast H_2O total column density product from GOME—Validation with in-situ aircraft measurements, *Atmos. Chem. Phys.*, *3*, 651–663.

Wagner, T., B. Dix, C. V. Friedeburg, U. Frieß, S. Sanghavi, R. Sinreich, and U. Platt (2004), MAX-DOAS O4 measurements: A new technique to derive information on atmospheric aerosols - Principles and information content, *J. Geophys. Res.*, *109*, 1–19, doi:10.1029/2004JD004904.

Wagner, T., M. O. Andreae, S. Beirle, S. Dorner, K. Mies, and R. Shaiganfar (2013), MAX-DOAS observations of the total atmospheric water vapour column and comparison with independent observations, *Atmos. Meas. Tech.*, *6*, 131–149, doi:10.5194/amt-6-131-2013.

Werner, C., P. J. Kelly, M. Doukas, T. Lopez, M. Pfeffer, R. McGimsey, and C. Neal (2013), Degassing of CO_2, SO_2, and H_2S associated with the 2009 eruption of Redoubt volcano, Alaska, *J. Volcanol. Geotherm. Res.*, *259*, 270–284, doi:10.1016/j.jvolgeores.2012.04.012.

Wiederhold, P. R. (1997), *Water Vapor Measurement: Methods and Instrumentation*, 384 pp., CRC Press, New York.

Wilson, L., R. S. J. Sparks, and G. P. L. Walker (1980), Explosive volcanic eruptions: IV. The control of magma properties and conduit geometry on eruption column behaviour, *Geophys. J. R. Astron. Soc.*, *63*, 117–148, doi:10.1111/j.1365-246X.1980.tb02613.x.

Woods, A. W. (1995), The dynamics of explosive volcanic eruptions, *Rev. Geophys.*, *33*(4), 495–530, doi:10.1029/95RG02096.

Yamaguchi, Y., A. B. Kahle, H. Tsu, T. Kawakami, and M. Pniel (1998), Overview of Advanced Spaceborne Thermal Emission and Reflection Radiometer (ASTER), *IEEE Trans. Geosci. Remote Sens.*, *36*(4), 1062–1071, doi:10.1109/36.700991.

Ye, H., E. J. Fetzer, D. H. Bromwich, E. F. Fishbein, E. T. Olsen, S. L. Granger, S. Y. Lee, L. Chen, and B. H. Lambrigtsen (2007), Atmospheric total precipitable water from AIRS and ECMWF during Antarctic summer, *Geophys. Res. Lett.*, *34*, L19701, doi:10.1029/2006GL028547.